

LOW ENERGY PHOTON MIMIC OF THE TRITIUM BETA DECAY ENERGY SPECTRUM

By

Neville Malabre-O'Sullivan

A THESIS SUBMITTED IN PARTIAL FULFILLMENT
OF THE REQUIREMENTS FOR THE DEGREE OF

Master of Applied Science

In

Nuclear Engineering

Faculty of Energy Systems and Nuclear Science

University of Ontario Institute of Technology

April, 2013

ABSTRACT

Tritium is a radioactive hydrogen isotope that is typically produced via neutron interaction with heavy water (D_2O), producing tritiated water (DTO). As a result of this, tritium accounts for roughly a third of all occupational exposures at a CANDU type nuclear power plant. This identifies a need to study the biological effects associated with tritium (and low energy electrons in general). However, there are complications regarding the dosimetry of tritium, as well as difficulties in handling and using tritium for the purposes of biophysics experiments. To avoid these difficulties, an experiment has been proposed using photons to mimic the beta decay energy spectrum of tritium. This would allow simulation of the radiation properties of tritium, so that a surrogate photon source can be used for biophysics experiments.

Through experimental and computational means, this work has explored the use of characteristic x-rays of various materials to modify the output spectrum of an x-ray source, such that it mimics the tritium beta decay spectrum. Additionally, the resultant primary electron spectrum generated in water from an x-ray source was simulated. The results from this research have indicated that the use of characteristic x-rays is not a viable method for simulating a tritium source. Also, the primary electron spectrum generated in water shows some promise for simulating tritium exposure, however further work must be done to investigate the slowing down electron spectrum.

Keywords: Tritium, MCNP, low energy electrons, biophysics, characteristic x-rays

ACKNOWLEDGEMENTS

I would like to first express my sincere gratitude towards Dr. Anthony Waker, who has been a fantastic mentor and supervisor throughout the course of my graduate studies. I thank him for the opportunities he has afforded me, and for his guidance, support and patience.

I would like to thank all the professors and staff of the Faculty of Energy Systems and Nuclear Science for all their assistance.

I would like to thank my friends and colleagues for their continued support and words of encouragement. Special thanks go to Fawaz Ali for his friendship and insights on radiation transport in MCNP.

I am grateful to the Natural Sciences and Engineering Council of Canada (NSERC) and the University Network of Excellence in Nuclear Engineering (UNENE) for their financial contributions to this research.

Lastly, my close friends and family have been overwhelmingly supportive of me and my academic endeavors, and for that I am truly thankful. In particular, I would like to thank my parents, Neville Sr. and Naleen, whose continued love and support has been a source of motivation and inspiration for me throughout the course of my life.

TABLE OF CONTENTS

ABSTRACT	ii
ACKNOWLEDGEMENTS.....	iii
LIST OF TABLES	vi
LIST OF FIGURES.....	vii
LIST OF ACRONYMS.....	x
NOMENCLATURE.....	xi
CHAPTER 1: INTRODUCTION	1
1.1 Thesis Objectives	6
1.2 Outline of Thesis.....	10
CHAPTER 2: THEORETICAL BACKGROUND.....	11
2.1 Photon Interaction with Matter	11
2.1.1 Photoelectric Effect.....	14
2.1.2 Compton Effect.....	16
2.1.3 Characteristic X-Rays	17
2.2 Electron Interaction with Matter	20
2.3 Monte Carlo Radiation Transport.....	23
2.3.1 Photon Transport in MCNP	24
2.3.2 Electron Transport in MCNP	27
CHAPTER 3: EXPERIMENTAL AND MODELING METHODOLOGY	29
3.1 Experimental Apparatus	29
3.1.1 X-Ray Generator	29

3.1.2	X-Ray Detector	34
3.1.3	Target Materials	36
3.1.4	Experimental Setup	37
3.2	Modelling Methodology	39
CHAPTER 4:	RESULTS AND DISCUSSION.....	42
4.1	Theoretical Predictions.....	42
4.2	Characteristic X-Ray Simulation Results	47
4.2.1	Composite Target.....	47
4.2.2	Mini-X Simulations	54
4.3	Detector Analysis	57
4.4	X-Ray Spectroscopy	60
4.5	Characteristic X-Ray Experimental Results	63
4.6	Electron Spectrum in Water	66
CHAPTER 5:	CONCLUSIONS.....	71
APPENDIX A:	RAW DATA TABLES	74
APPENDIX B:	DOCUMENTATION FOR MINI-X REGISTRATION.....	76
APPENDIX C:	MCNP CODES WRITTEN FOR THESIS.....	84
REFERENCES	88

LIST OF TABLES

1.1	ICRP Recommended Radiation Weighting Factors	2
2.1	Characteristic X-Ray Nomenclature.....	18
3.1	Characteristic x-ray energies, thickness and yield for materials.....	37
4.1	Physical data for target materials	43
4.2a	Fluorescent Rate results for iron	44
4.2b	Fluorescent Rate results for titanium.....	44
4.3a	Simulation results for iron	45
4.3b	Simulation results for titanium.....	45
4.4	Simulation results for composite target	52
4.5	List of Mini-X filters	60

LIST OF FIGURES

1.1	Relative Beta Decay Spectrum of Tritium.....	6
1.2	Photon interaction probabilities based on energy and atomic number	8
1.3	General method for simulating tritium exposure	9
2.1	Range of Electromagnetic Radiation	11
2.2	X-rays incident on a material of thickness t	12
2.3	Illustration of the photoelectric effect.....	14
2.4	Illustration of Compton scattering	16
2.5	Photoelectric versus Compton interaction cross section data for water	17
2.6	Illustration of characteristic x-ray emission	18
2.7	Fluorescent yields for various materials.....	19
2.8	Typical radiation transport problem	23
3.1	X-ray tube schematic.....	29
3.2	Mini-X x-ray source.....	31
3.3	Mini-X Output Spectra at various operating voltages.....	32
3.4	Mini-X accessories.....	33
3.5	Comparison of filtered and unfiltered spectra	34
3.6	X-123 x-ray detector	35
3.7	Data acquisition software	36
3.8	Target materials	36
3.9	Experimental setup.....	37
3.10	Mini-X's interlock and LED.....	38

3.11	Schematic of circuit that controls interlock.....	39
3.12	Illustration of characteristic x-ray model.....	40
4.1	Illustration of Mini-X irradiation area.....	43
4.2a	X-ray spectrum for composition of 80% iron, 20% titanium.....	48
4.2b	X-ray spectrum for composition of 70% iron, 30% titanium.....	49
4.2c	X-ray spectrum for composition of 60% iron, 40% titanium.....	49
4.2d	X-ray spectrum for composition of 50% iron, 50% titanium.....	50
4.2e	X-ray spectrum for composition of 40% iron, 60% titanium.....	50
4.2f	X-ray spectrum for composition of 30% iron, 70% titanium.....	51
4.2g	X-ray spectrum for composition of 20% iron, 80% titanium.....	51
4.3	Plot of titanium atom fraction versus count ratio.....	52
4.4	Approximate Mini-X output spectrum at 20 kV _p	54
4.5	Simulation x-ray spectra for iron.....	55
4.6	Simulation x-ray spectra for titanium.....	55
4.7a	Simulation x-ray spectra for composite target.....	56
4.7b	Simulation x-ray spectra for composite target (close up).....	56
4.8	Energy resolution versus peaking time.....	58
4.9	Experimental analyses of peaking time and energy resolution.....	59
4.10	Unfiltered Mini-X spectrum at 20 kV _p	61
4.11	Filtered Mini-X spectrum at 20 kV _p	62
4.12a	Experimental x-ray spectra for iron.....	64
4.12b	Experimental x-ray spectra for titanium.....	64

4.13a	Comparison of simulated and experimental spectra for iron	65
4.13b	Comparison of simulated and experimental spectra for titanium.....	65
4.14	Spectral comparison of Mini-X and tritium.....	66
4.15	Comparison of simulated x-ray spectrum with filtered spectrum	67
4.16a	Electron spectrum for 2 mm water slab.....	68
4.16b	Electron spectrum for 3 mm water slab.....	68

LIST OF ACRONYMS

SI	International System of Units
ICRP	International Commission of Radiological Protection
CANDU	Canadian Deuterium Uranium
OBT	Organically Bound Tritium
RBE	Relative Biological Effectiveness
MCNP	Monte Carlo N-Particle Code
XRF	X-Ray Fluorescence
MCA	Multi-Channel Analyzer

NOMENCLATURE

$D_{T,R}$	Average absorbed dose within a medium, Gy
w_R	Radiation weighting factor
D_R	Reference dose for RBE determination, Gy
D_T	Test dose for RBE determination, Gy
Z	Atomic number of an element
P	Probability of photon interacting with material at a distance x
I_0	Incident x-ray intensity, keV s^{-1}
I	Outgoing x-ray intensity, keV s^{-1}
t	Material thickness, cm
μ	Linear attenuation coefficient, cm^{-1}
E_K	Kinetic energy of photoelectron, keV
h	Planck's constant, 6.626×10^{-34} J s
ν	Photon frequency, s^{-1}
E_b	Binding energy of atomic electron, keV
τ	Probability of photon undergoing photoelectric absorption
m_e	Electron mass, 9.109×10^{-31} kg
c	Speed of light, 2.998×10^8 m/s
e	Electron charge, 1.6×10^{-19} C
β	Ratio of particle velocity to the speed of light
μ_m	Mass attenuation coefficient, cm^2/g
ρ	Material density, g/cm^3

F	Fluorescence rate, s ⁻¹
ω	Fluorescent yield
τ_d	Dead time, s
τ_p	Peaking time, s

CHAPTER 1

INTRODUCTION

The discovery of radiation and radioactive materials has had a profound impact in both science and engineering, which have led to many practical applications, most notably in medicine and energy production. However, though radiation has enriched our livelihood in many ways, it is important to remember that it can have adverse effects on the human body. Radiation is typically classified as non-ionizing or ionizing. Non-ionizing radiation is a type of electromagnetic radiation (photons) that does not carry enough energy to remove an electron from an atom or molecule. At some frequencies however, it can excite electrons or cause atoms and molecules to vibrate. Familiar examples of this type of radiation are microwaves, infrared and ultraviolet radiation [1]. Ionizing radiation, on the other hand, is radiation that carries enough energy to remove an electron from an atom or molecule and break chemical bonds. Radiation of this type can be in the form of charged (ie. electrons, protons) or uncharged (photons, neutrons) particles [1]. Though both types of radiation can lead to adverse biological effects, ionizing radiation is generally of greater concern as it is considered far more damaging to the basic components of living organisms, such as molecules and cells [36]. Since the risk to our health is greater, it is important to understand how ionizing radiation interacts with biological matter, and to take preventative measures from being overexposed to it. Investigation into the risks of radiation exposure is primarily carried out by health physicists and radiation biologists.

The *absorbed dose* is defined as the energy deposited by ionizing radiation per unit mass in a medium. The unit for absorbed dose is the Gray (Gy)¹, which has the SI units J/kg [2]. On its own, absorbed dose cannot be used to assess the health risks for a given exposure, as some radiation types carry greater risks than others per unit dose. For example, alpha particles are more damaging than photons per unit dose, due to the fact that they deposit their energy over a smaller range, which leads to a higher ionization density². To address this, a quantity called the *equivalent dose*, H_T , is used which is related to the absorbed dose by [3]:

$$H_T = \sum_R D_{T,R} * w_R \quad 1.1$$

Where $D_{T,R}$ is the average absorbed dose in a medium, for a certain radiation type, and w_R is the radiation weighting factor. The radiation weighting factor is used to account for the fact that some radiation types carry a greater risk than others. The unit for equivalent dose is the Sievert (Sv), which has the same SI units as the Gray. Table 1.1 below shows the radiation weighting factors that are recommended in the ICRP Publication 103 (2007) for various radiation types [3]:

Radiation Type	w_R
Photons	1
Electrons and muons	1
Protons and Charged Pions	2
Alpha particles, fission fragments, heavy nuclei	20

Table 1.1. Recommended radiation weighting factors

¹ The old unit for absorbed dose is the rad [2], where 1 rad = 0.01Gy

² Ionization density is defined as the number of ions created per unit path length

The radiation weighting factor for neutrons has been omitted from Table 1.1 as it is a function of neutron energy [3]. For moderate to high doses, it has been found that the weighting factors recommended by ICRP provide a good estimate for equivalent dose and risk assessments. However, there are still many uncertainties about the risks for low dose radiation, and appropriate weighting factors are an important aspect of this uncertainty. In particular, as shown in Table 1.1, the weighting factor for electrons is recommended by ICRP to be unity. However, there is some evidence from tritium studies that suggest that the weighting factor for electrons may be greater than 1 at low electron energies [9]. In fact, according to ICRP Publication 103 [3], "Heterogeneity of the radiation dose within cells, as can occur with tritium or Auger emitters incorporated into DNA, may also require specific analysis." Based on these remarks, there are grounds for further investigation into low energy radiation exposure.

Tritium is of particular interest because a) it is a low energy beta emitter and b) it is a by-product of CANDU nuclear power plant operations. CANDU type nuclear power plants are moderated and cooled with deuterium oxide (D_2O), also known as heavy water. Deuterium is an isotope of hydrogen, having one proton and one neutron in its nucleus. When a deuterium atom is able to capture a neutron, it becomes a radioactive isotope of hydrogen known as tritium [4]. It decays via emission of a beta particle, with a half-life of 12.32 years, which is the time it takes for some substance to decay to half its initial value. The emitted beta particle has an average energy of 5.67 keV and a maximum energy of 18.6 keV. This beta particle is

not energetic enough to pass through the dead layer of skin, so tritium poses no external health risks; however, if it gets inside the body there will be an internal exposure to unprotected cells and thus a potential health risk [5]. Tritium beta particles have a maximum range of 6 μm and an average range of 1 μm in tissue [5]. Therefore, a tritium beta particle will deposit all of its energy locally, which can lead to cell damage through the direct ionization of important biomolecules and the production of free radicals [2]. Also, since tritium is chemically identical to hydrogen, it can bind itself to organic materials in the body. The biological half-life is defined as the time it takes for half of some substance to be biologically removed from the body [2]. For tritium, the biological half-life is typically 10 days, but for organically bound tritium (OBT), it can be as high as 40 days [5], which would add to the potential risk. It is important to note that tritium accounts for roughly 30% of all occupational exposures at a CANDU power plant [6]. Given the exposure to workers and the underlying uncertainties regarding low dose exposures from low energy electrons, it is important that further studies on tritium dosimetry and radiation quality are carried out.

As mentioned previously, some radiation types (ie. photons, electrons, neutrons) carry greater risks than others, which is why radiation weighting factors are necessary. A useful way to compare different radiation types is to determine the relative biological effectiveness (RBE). This quantity is defined as the ratio of the dose of a reference radiation, D_R , needed to produce the same biological effects as seen with the dose of a test radiation, D_T [7]:

$$RBE = \frac{D_R}{D_T} \quad 1.2$$

Different radiation types will generally have different biological effects because they transfer energy differently. RBE studies have been performed for tritium, where the reference radiation was either x-rays or gamma rays, some of which have reported RBE values greater than unity³. However, when studying the biological effectiveness of tritium, researchers have had to use some form of *tritiated* gas (HT) or water vapour (HTO), which has certain limitations for biophysics experiments. One issue is that a radioactive gas or vapour is difficult to handle and contain, which also increases the risk of accidental exposure. Another issue is that the exact duration of an exposure is largely unknown, and doses have to be estimated. Lastly, the sample is usually uniformly irradiated by the tritiated substance, which is an issue if partial irradiation of a sample is required. With these limitations in mind, the primary goal of this thesis is to determine if there is a more practical means by which one can study the biological effects of tritium in a reproducible and methodical fashion.

³ See reference 8, 9 and 10 for tritium RBE studies

1.1 Thesis Objectives

Figure 1.1 shows the relative tritium beta decay energy spectrum. The raw data for the spectrum was obtained from the Radiological ToolBox software [11] and can be seen in Appendix A. For a given tritium intake, the energy of the beta particles (electrons) produced will have an energy distribution similar to the one seen in Figure 1.1.

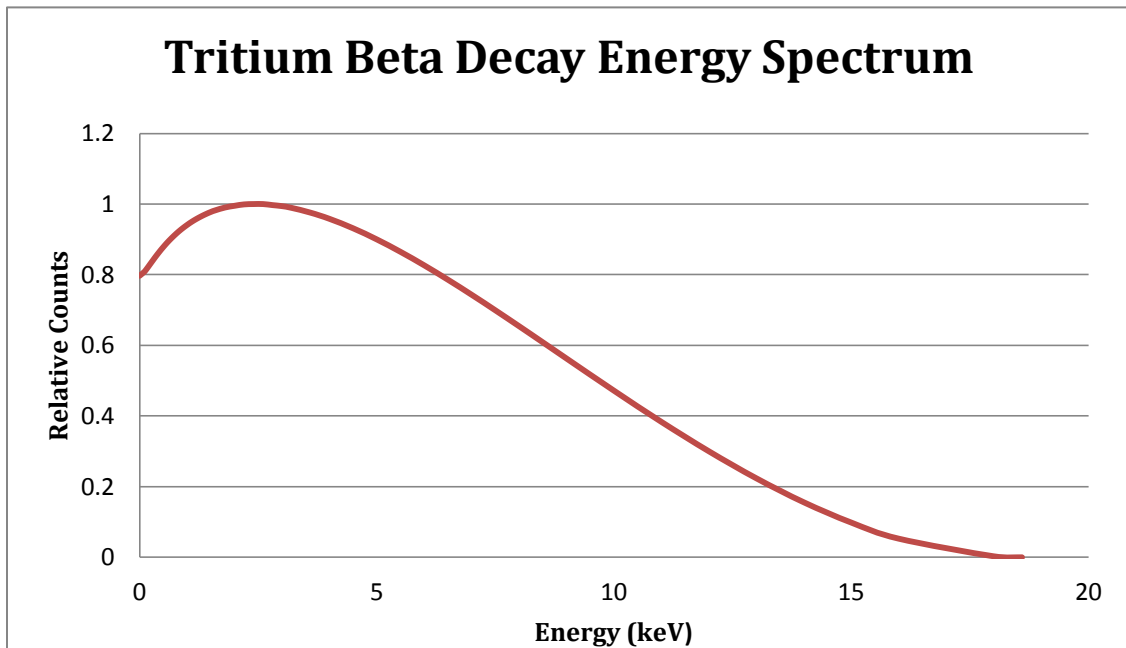


Figure 1.1 Relative Beta Decay Spectrum of Tritium [11]

The goal of this thesis is to explore if low energy photons can be used to generate an electron spectrum in tissue that mimics the beta spectrum of tritium in tissue. To elucidate this idea, consider the interaction of photons in water (a tissue-like substance). An electron bound to a water molecule can gain kinetic energy due to the direct interaction from the incident photon. The energy it receives will depend on the type of interaction and the energy of the incident photon. The electron will then go on to transfer its energy to the water, causing further ionizations in the

medium [12]. Since beta particles deposit their energy in a similar manner as electrons [12], simulating a tritium exposure in tissue with photons should produce the same effect as an actual tritium exposure. Recalling the limitations of using tritium gas or tritiated water for biophysics experiments, using a photon source has the following advantages:

- No issues handling a radioactive gas or vapour
- Exact duration of exposure will be known, since the beam can be turned on and off at will
- Using a narrow photon beam allows for partial irradiation of a sample.

This thesis will investigate methods for simulating a tritium exposure in water (or tissue) with the use of photons (x-rays), through experimental and computational means. In order to properly simulate this exposure, it is important to know how the photons will transfer their energy when they interact. A photon will typically undergo one of three types of interactions⁴: Photoelectric absorption, Compton scatter or pair production [2]. Figure 1.2 is a plot that indicates which interaction type is more probable based on the photon energy and the material it is interacting with.

⁴ Photons can also interact via Thomson or Rayleigh scattering, but for the energies considered, the interactions discussed are much more likely.

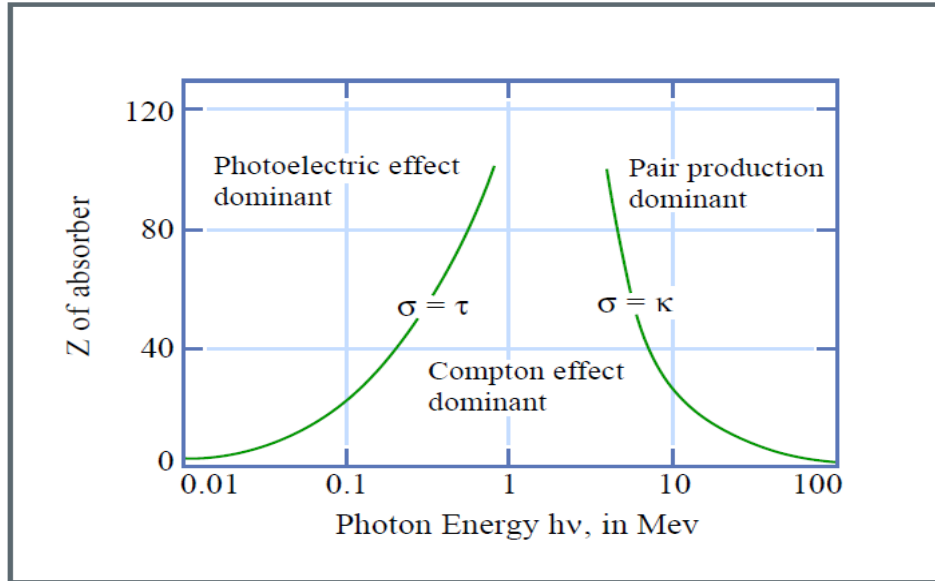


Figure 1.2 Photon Interaction probabilities based on energy and atomic number [13]

The curved lines indicate where two interaction types are equally probable. Given that the maximum photon energy needed to mimic tritium is 18.6 keV, and that water and tissue are low Z materials, it is determined that the majority of photons will interact via the photoelectric effect, and some via the Compton effect. When a photon undergoes a photoelectric interaction with an electron, it will transfer all of its energy to the electron [13]. The kinetic energy gained by the electron will be the difference between its binding energy and the energy of the incident photon. For an electron bound to a water molecule, its binding energy is about 12.6 eV [21]. This is roughly three orders of magnitude lower than the photon energies considered for this thesis, so to a good approximation, for photoelectric interactions, the electron energy will be the same as the incident photon energy. With these processes in mind, it is clear that if the photon spectrum matches the tritium beta decay energy spectrum, then the photoelectron spectrum generated in water will also match the

tritium beta spectrum. Therefore, the main focus of this thesis will be on the output spectrum of the photon source. Figure 1.3 illustrates the proposed method for mimicking a tritium beta spectrum.

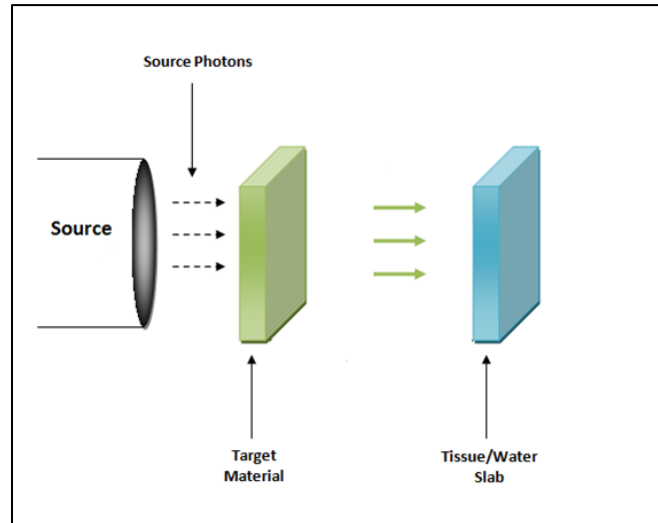


Figure 1.3 General method for simulating tritium exposure

In principle, the photon spectrum (green arrows) has to match the tritium beta decay spectrum from Figure 1.1, to generate the necessary electron spectrum in water. The output spectrum from the photon source alone, however, will not match the required spectrum; therefore, methods to modify the source spectrum must also be investigated. Thus, this thesis will also explore the use of a target material's characteristic x-rays in modifying the energy spectrum of a photon source, such that it more closely matches that of a tritium beta decay energy spectrum.

1.2 Outline of Thesis

This thesis will explore the use of photons for simulating tritium exposures in water and tissue samples. Chapter 1 serves as an introduction to some concepts in health physics, uncertainties in the weighting factor for low energy electrons, and establishes the goals and purpose for this research. Chapter 2 will elucidate the theoretical principles regarding the interaction of photons and electrons with matter, as well as outline the transport of these particles in the Monte Carlo N-Particle (MCNP) transport code. This chapter will also give an overview on the syntax and specifications regarding the MCNP code. In Chapter 3, the experimental apparatus and the modeling methods will be discussed. This chapter will give the background and operating principles for the equipment used, and outline the methodology for the MCNP simulations. Chapter 4 will outline and discuss the results obtained from computational and experimental work. Finally, in Chapter 5, conclusions will be drawn from the results discussed in Chapter 4, and ideas for further work will be recommended.

CHAPTER 2 THEORETICAL BACKGROUND

2.1 Photon Interaction with Matter

According to the standard model of particle physics, photons are massless, uncharged elementary particles that mediate the electromagnetic force, and are thus the source of all forms of electromagnetic radiation [19]. They typically have different characterizations based on their energy, ranging from radio waves to gamma rays. Figure 2.1 below displays the different types of electromagnetic radiation.

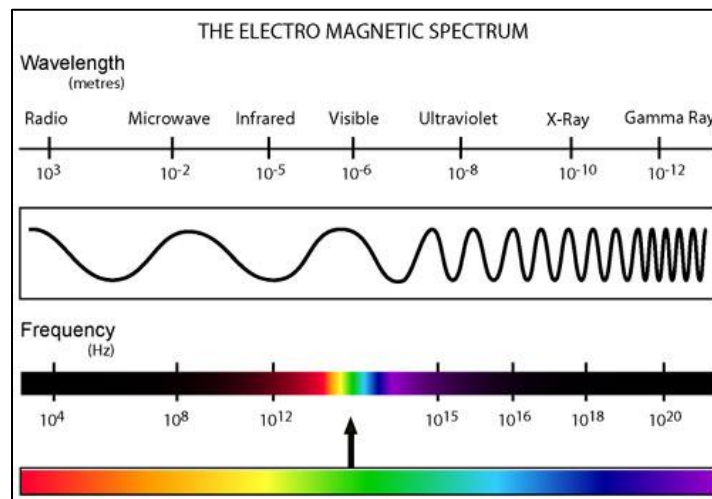


Figure 2.1 Range of Electromagnetic Radiation [15]

Since a photon source is to be used to simulate the beta spectrum of tritium, it is important to explore how photons interact with matter. This thesis will only consider photons in the x-ray region of the electromagnetic spectrum, since their energies are more comparable to the energy range of tritium beta particles.

When a photon is incident on some target material, it can be absorbed, scattered or transmitted [2]. When it is absorbed, it is not detectable on the other side of the target, thus transferring all of its energy to the material. If it is scattered, it will leave the other side of the target with a different angle and energy than it had when it entered, transferring the energy lost to the target material. Lastly, a photon can also pass through the material without interacting with it at all. When a collection of photons are incident on a target, they can interact in any one of these three ways, and it is essentially impossible to predict how a particular photon will interact with the material. However, it is possible to determine the probability, P , that a photon can pass through the material without interacting. Consider a slab of material with thickness t , as shown in Figure 2.2.

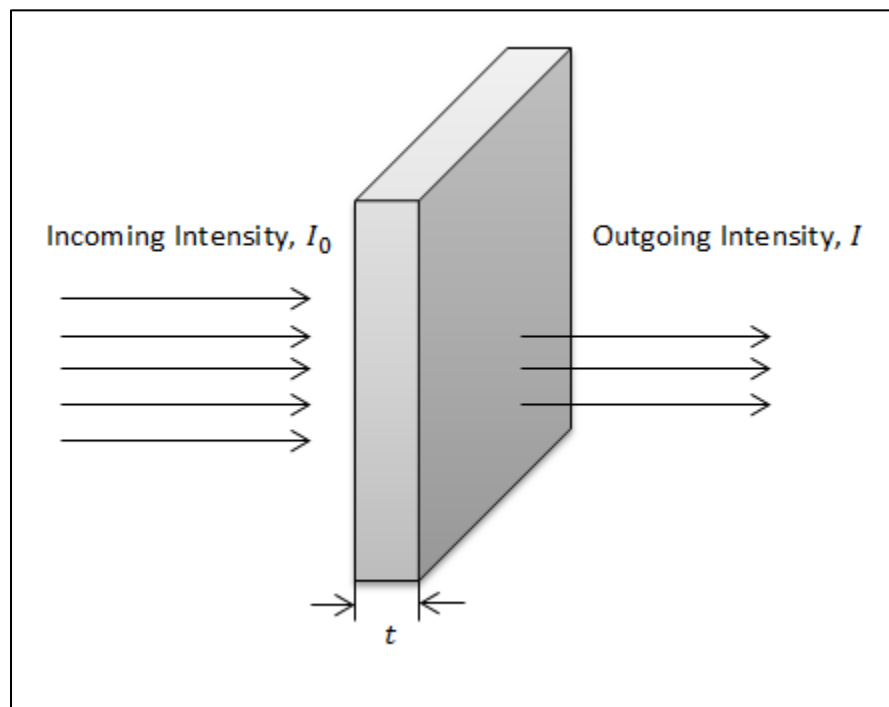


Figure 2.2 X-rays incident on a material of thickness t

If the intensity of the photons entering the material is known, then the intensity of the photons escaping the material can be determined. This phenomenon where the intensity changes as photons pass through some material is known as attenuation. The intensity, I , traversing a distance x through some material before interacting, is related to the incoming intensity, I_0 , by [13]:

$$I = I_0 e^{-\mu x} \quad 2.1a$$

Where μ is the linear attenuation coefficient, which is an energy dependent quantity, and x is the distance travelled by the photon. The probability of a photon undergoing an interaction at a distance x within the material is given by slightly rearranging Equation 2.1a:

$$P = \frac{I}{I_0} = e^{-\mu x} \quad 2.1b$$

Substituting in t for x in Equation 2.1b gives the probability that a photon can traverse through the material without interacting with an atom. Most tables report the attenuation coefficient for a material in terms of the material density; this is known as the mass attenuation coefficient, μ_m . This is related to the linear attenuation coefficient by:

$$\mu = \mu_m * \rho \quad 2.2$$

Where ρ is the density of the target material. Equation 2.1b gives insight to the number of photons transmitted through some material, which in turn determines the number of photons interacting within the material. However, Equation 2.1b does not indicate how these photons will interact with the material. For this, consideration of the ways in which photons interact with matter must be taken into

account. Recall from Chapter 1 that for the energy ranges considered for this thesis (approximately 1 to 18.6 keV), the main interaction types will be the photoelectric effect and Compton scattering, so only these two processes will be considered. Pair production has a threshold of 1.022 MeV, which is much higher than the energies being considered for this study.

2.1.1 Photoelectric Effect

The photoelectric effect occurs when a photon transfers all of its energy to an electron in some medium. This process is illustrated in Figure 2.3.

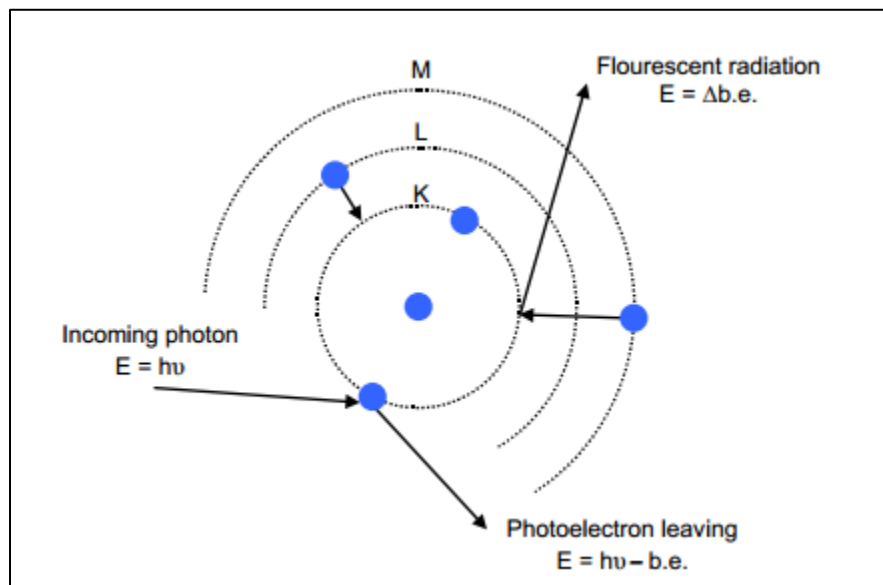


Figure 2.3 Illustration of the photoelectric effect [13]

If the incoming photon has sufficient energy, it can free a tightly bound electron from its shell, and at this point it becomes a photoelectron. The energy that it will carry off is given by [13]:

$$E_K = h\nu - E_b \quad 2.3$$

Where E_K is the kinetic energy of the photoelectron, h is Planck's Constant, ν is the frequency of the incoming photon and E_b is the minimum energy required to liberate an electron from an atom, also known as the *binding energy* [13]. Once the photoelectron has acquired this kinetic energy, it will leave the atom it was bound to and likely deposit its energy within the medium through further ionizations and excitations. The photoelectron leaves a vacancy in its atom that will subsequently be filled by an electron from a higher shell. When an electron moves from a higher shell to a lower shell, it emits a photon which is known as a fluorescent photon; emissions of this type are also known as characteristic x-rays, and will be explored later. With the emission of a fluorescent photon, one of two things can occur; this photon can leave the atom, or it will transfer its energy to an electron in a higher shell, causing an additional ionization of the atom. Electrons that are emitted following the interaction with a fluorescent photon are called Auger electrons. The probability, τ , of a photon (x-ray in particular) undergoing photoelectric absorption is roughly proportional to [13]:

$$\tau \sim \frac{Z^n}{(h\nu)^3} \quad 2.4$$

Where n varies between 3 and 4, depending on the energy.

2.1.2 Compton Effect

The Compton effect differs from the photoelectric effect in the way that a photon transfers its energy. The Compton effect is where an incident photon, of energy E , scatters off an atomic electron. After the scattering process, the photon is deflected at an angle θ and carries off an energy E' ; the energy lost by the photon is transferred to the electron. Figure 2.4 illustrates this process.

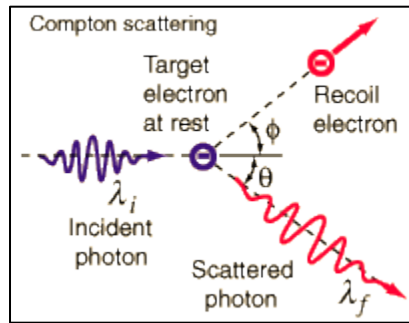


Figure 2.4 - Illustration of Compton scattering [16]

The incident photon will usually scatter off an electron whose binding energy is much lower than that of the photon energy [13]. The equation for the resultant energy carried off by the scattered photon is given by [2]:

$$E' = \frac{E}{1 + \frac{E}{m_e c^2} (1 - \cos\theta)} \quad 2.5$$

Where m_e is the mass of the electron, c is the speed of light and θ is the deflection angle of the scattered photon. For the photon energies considered in this thesis, the Compton scattering process will not transfer much energy to the electron [13]. As an example, consider an 18 keV photon undergoing a maximum energy transfer Compton interaction ($\theta = 180^\circ$). The scattered photon will carry off an energy of about 16.8 keV, giving the electron an energy of 1.18 keV. Therefore, the Compton

interactions in water will produce low energy electrons, which are required in order to mimic tritium. However, since the Compton interaction cross section is lower than the photoelectric cross section at these energies (see Figure 2.5), it is likely that the ratio of Compton interactions to photoelectric absorption in water will be minute.

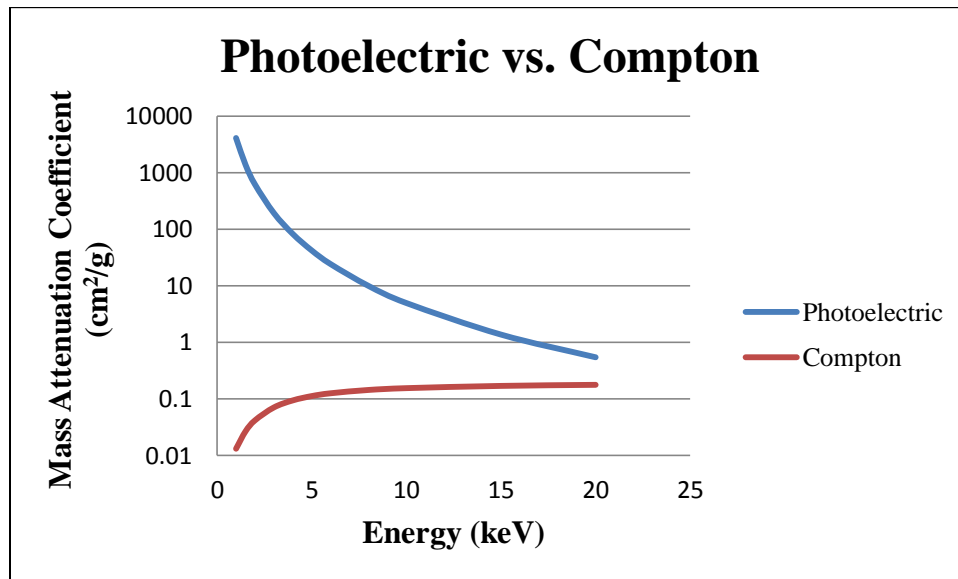


Figure 2.5 Photoelectric versus Compton interaction cross section data for water [18]

2.1.3 Characteristic X-Rays

Recall that a photon with sufficient energy can liberate an electron from its atomic shell, leaving a vacancy in its place. This is illustrated in Figure 2.6. Suppose an incident x-ray of energy E interacts with an electron in an energy state, E_0 , and ejects it. The ejected electron will carry off energy $(E - E_0)$, and leave a vacancy in its place. An electron from a higher shell, of energy E_1 , will drop down to fill the vacancy, and in doing so emits a secondary x-ray with energy $(E_1 - E_0)$. Secondary

x-rays that are produced in this manner are emitted isotropically [20]. These secondary x-ray emissions are called *characteristic* because the energy they carry off is unique for each atom [2]. This uniqueness in energy is valuable to this work, because the characteristic x-ray output of some materials may allow modification of the output spectrum of an x-ray source so that it more closely matches the tritium spectrum.

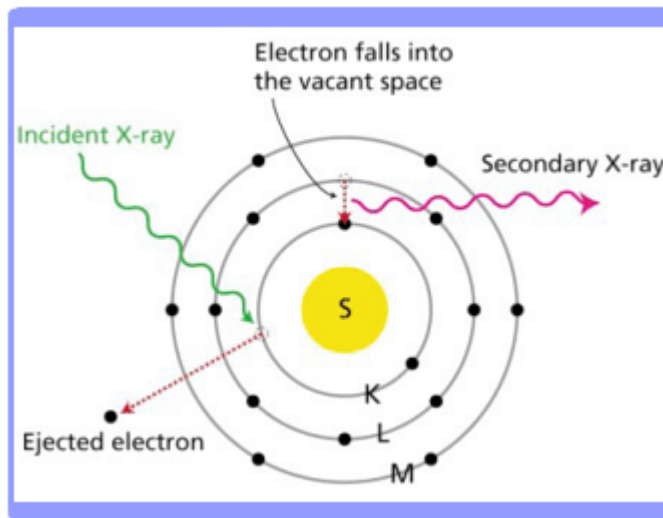


Figure 2.6 Illustration of characteristic x-ray emission [22]

Figure 2.6 shows that each electron shell has a designated letter (ie. K, L, M and so on). An incident photon can interact with an electron in any shell, however, K shell excitations are the most probable origin of a photoelectron if the incoming photon has sufficient energy [13]. Table 2.1 shows how characteristic x-rays are designated based on the shell transition.

Transition	X-ray Nomenclature
L → K	K_{α}
M → K	K_{β}
M → L	L_{α}
N → L	L_{β}

Table 2.1 Characteristic x-ray Nomenclature

As noted earlier, the emitted characteristic x-ray can either leave the atom, or interact with an electron in a higher shell and produce an Auger electron. The fluorescent yield is a quantity that is defined as the probability that an inner shell ionization will result in the emission of a characteristic x-ray (ie. leave the atom) [2]. The graph in Figure 2.7 shows the fluorescent yield versus the atomic number. In this figure, K-shell and L-shell correspond to ionizations occurring in the K and L shell respectively. As shown in Figure 2.7, the fluorescent yield for K shell ionizations increases very rapidly with increasing atomic number. Materials should be chosen such that their characteristic x-ray energies lie within the range required, and that they have “adequate” fluorescent yields. Figure 2.7 and data on characteristic x-ray energies will facilitate selection of the best materials.

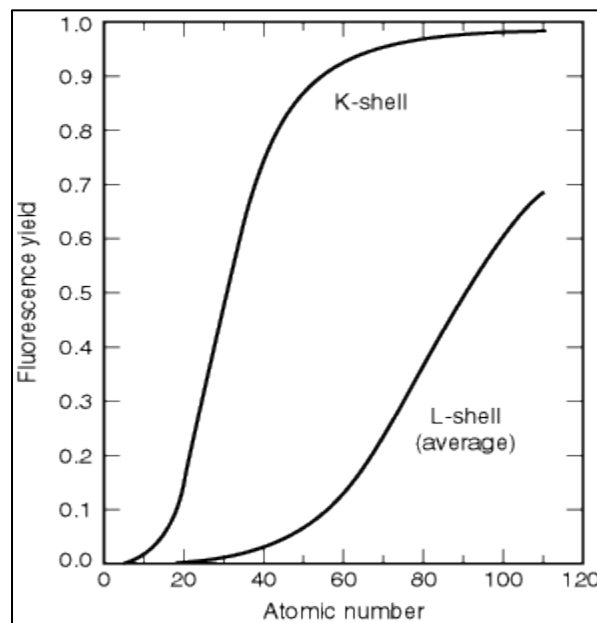


Figure 2.7 Fluorescent yields for various materials [35]

It should be noted that due to the structure of the atom, the electron energies in the shells above K are not degenerate. This means that an atom's L shell for

example, is subdivided into three distinct energy shells (LI, LII and LIII). Therefore, the L→K transition is actually LIII→K and LII→K⁵, both of which emit distinct K x-ray energies [2]. However, the energy differences for the materials being used for this thesis are negligible, so the transitions as indicated in Table 2.1 are valid.

2.2 Electron Interaction with Matter

The electron is an elementary particle that is negatively charged and is one of the fundamental constituents of atoms, along with protons and neutrons. Since the electron is a charged particle, its interaction is fundamentally different from the interactions of uncharged particles, such as photons and neutrons. The transport of neutral particles is essentially characterized by infrequent isolated collisions as they interact with matter [16]. Electrons on the other hand are continuously subjected to long-range Coulomb forces as they are traverse through some material. As an example, a photon undergoing an energy loss from 0.5 MeV to 0.0625 MeV will likely experience fewer than 10 interactions, while an electron over the same energy loss will have about 10^5 individual interactions [16]. As discussed later, this makes transporting electrons a difficult task for modeling purposes. As with photons, the interaction of electrons with matter is essentially based on how they transfer (or deposit) their energy in some medium. The mechanism by which electrons transfer their energy is known as the stopping power, which is defined as the average energy lost per unit path length [2]; for electrons, the stopping power can be collisional or radiative.

⁵ Quantum *selection rules* forbid the LI→K transition. See ref. [19] for more.

Electrons can lose energy through collisions with atomic electrons, which can lead to ionizations and excitations in the medium [35]. Electrons that are liberated through electron impact collisions are called knock-on electrons. The relative importance between ionization and excitation increases very rapidly with the energy of the electron (ie. ionizations more prevalent at higher energies). As an electron passes through some material, it can lose no more than half of its energy in a single collision [14]. According to quantum mechanics, the outgoing electrons from such a collision are indistinguishable; therefore, the electron with the lower energy after a collision is treated as the impacted electron [2]. The collisional stopping power describes the energy loss due to direct collisions with atomic electrons; for relativistic electrons, it is given by [2]:

$$-\left(\frac{dE}{dx}\right)_{col} = \frac{1}{(4\pi\epsilon_0)^2} \frac{2\pi e^4 n}{m_e v^2} \left(\ln \left(\frac{(m_e c^2)^2 \epsilon^2 (\epsilon + 2)}{2I^2} \right) + F(\beta) \right) \quad 2.5$$

$$F(\beta) = (1 - \beta^2) \left[1 + \frac{\epsilon^2}{8} - (2\epsilon + 1) \ln(2) \right]$$

Where:

ϵ_0 – Vacuum permittivity constant (8.854×10^{-12} F/m)

e – Electron charge (1.6×10^{-19} C)

n – Atom density (# of particles/cm³)

v – Velocity of particle (m/s)

ϵ – Ratio of kinetic energy to rest mass energy

I – Ionization potential or binding energy (MeV)

β – Ratio of velocity to the speed of light

An electron can be decelerated due to the electric field generated by the nucleus of an atom. This deceleration causes the atom to give off what is known as Bremsstrahlung radiation⁶ [2]. Bremsstrahlung radiation has a continuous energy spectrum, with an intensity that depends on the energy of the electron and the atomic number of the material it traverses. There is no analytical formula for the radiative stopping power, however, it can be approximated as a ratio to the collisional stopping power [2]:

$$\frac{(dE/dx)_{rad}}{(dE/dx)_{col}} \approx \frac{ZE}{800} \quad 2.6$$

Where E is the sum of the electron kinetic energy and its rest mass energy. This implies that radiative losses are only significant for high energy electrons and high Z materials. Since electrons will be produced in water, it's expected that radiative losses will be negligible.

⁶Bremsstrahlung radiation is also known as braking radiation

2.3 Monte Carlo Radiation Transport

Much of the analysis for this thesis was performed using the MCNP transport code, so it is important to outline the basics of how this code works and how it transports radiation. MCNP is a general purpose code that can transport neutrons, photons and electrons. The transport of radiation is a stochastic process, which makes MCNP (and Monte Carlo methods in general) a powerful tool for simulating radiation transport problems, since its algorithms rely on random sampling. Figure 2.8 is an example of a typical radiation transport problem in MCNP.

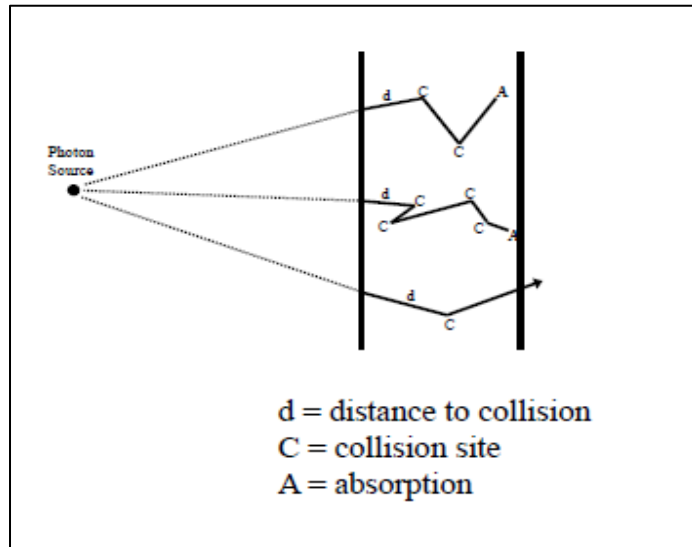


Figure 2.8 Typical radiation transport problem [22]

In this problem, photons are emitted at different angles, and undergo collisions within some medium. During a simulation, MCNP will randomly sample for where a particle will experience an interaction, direction after a collision and the type of interaction that will take place. MCNP treats each source particle as an independent random event, and will follow each particle throughout its history (life to death); the history of secondary particles can also be tracked. As the simulation progresses,

user defined quantities of interest (ie. energy deposition in a medium) are tallied, as well as the statistical precision of the results [17]. In order to simulate the problem in Figure 2.8, the user must create an input file that specifies some aspects of the transport problem, such as:

- Energy and direction of the source photons
- Geometrical and material makeup of the region where the photons are interacting
- Whether or not to track secondary particles
- Tally (detector) options important to the problem

The input file is therefore one of the more important aspects of the radiation transport problem. Appendix C shows some of the input files that were used for this thesis, and the details for these models in particular will be explored in chapter 3. For a more comprehensive overview on the structure and syntax of the input file, see reference 17. It should be noted that Monte Carlo methods use approximations to simulate the physics of radiation transport in some medium [17]. The remainder of this chapter will therefore focus on the transport of photons and electrons in MCNP.

2.3.1 Photon Transport in MCNP

In MCNP, a photon is transported by tracking its history as it moves through the medium. This is done by taking into account the distance it travels between collisions. It should be noted that photons have a low energy cut-off of 1 keV; if a photons energy drops below this lower limit, MCNP will stop tracking it, and deposit

the remaining energy locally. The distance to a collision is related to the macroscopic cross section, Σ_t , of the medium that the particle is being transported through. This quantity is interpreted as the probability per unit length that a particle will undergo a collision. The probability, P , that a particle will travel a distance x before experiencing a collision is given by [17]:

$$P(x) = e^{-\Sigma_t x} \quad 2.7$$

Note that this equation is almost identical to Equation 2.1b. In fact, for photons, the macroscopic cross is the same as the linear attenuation coefficient, so Equation 2.7 can be rewritten as Equation 2.1b:

$$P(x) = e^{-\mu x}$$

From here, the probability of a photon experiencing a collision between x and $x + dx$ is [17]:

$$P(x)dx = e^{-\mu x} \mu dx \quad 2.8$$

Setting the left side of Equation 2.8 to be a random number, ξ , on the interval [0,1) and integrating the right side, gives:

$$\xi = \int_0^l e^{-\mu x} \mu dx = 1 - e^{-\mu l}$$

Rearranging and solving for l :

$$l = -\frac{1}{\mu} \ln(1 - \xi) \quad 2.9$$

The term $(1 - \xi)$ is randomly distributed the same way that ξ is, so Equation 2.9 can be further simplified as:

$$l = -\frac{1}{\mu} \ln(\xi) \quad 2.9b$$

This equation is very dependent on the medium the photon is travelling through, so it is important for MCNP to keep track of the photon position with respect to the boundary surfaces of a given medium. To understand why this is important, consider a photon that is within some medium and has just undergone a collision. Using Equation 2.9b, MCNP will calculate the distance to the next collision point. If the distance to this collision point is less than the distance to a medium's surface crossing, then the photon will undergo a collision. If instead the distance to a collision is greater or equal to the distance to a surface crossing, the photon will cross the boundary, and MCNP will continue to track the photon's history at the surface crossing point. This is true for neutrons and electrons as well [17]. Photons will either undergo one of the two photon interaction types discussed earlier. In MCNP, the probability of a photon undergoing a certain interaction type is determined by the ratio of the cross section for that interaction type to the total cross section. Therefore, by using the cross section tables, MCNP can create a probability distribution, that can be sampled randomly to determine which interaction will occur [22]. The photoelectric cross section is roughly given by Equation 2.4; for Compton scattering, the cross section is described by the Klein-Nishina cross section, $K(\alpha, \mu)$ [17]:

$$K(\alpha, \mu)d\mu = \pi r_0^2 \left(\frac{\alpha'}{\alpha}\right)^2 \left[\frac{\alpha'}{\alpha} + \frac{\alpha}{\alpha'} + \mu'^2 - 1 \right] d\mu' \quad 2.10$$

Where r_0 is the Bohr radius, μ' is the cosine of the angle the incident photon was scattered off at and α and α' are related to the incident and final photon energies, respectively, by:

$$\alpha = \frac{E}{mc^2}$$

$$\alpha' = \frac{\alpha}{[1 + \alpha(1 - \mu)]}$$

For this thesis, MCNP uses Khan's method for sampling the Compton scattering process exactly [17].

2.3.2 Electron Transport in MCNP

As described in Section 2.2, the interactions of electrons with matter are more extensive than they are for photons, since they can undergo several interactions within a medium. This makes modeling every electron interaction particularly difficult and not feasible for some transport problems since it can be computationally taxing. Instead, MCNP makes use of some multiple scattering theories to simplify the transport of charge particles in general. However, these theories rely on a variety of approximations, so they cannot solve the entire transport problem.

MCNP employs a method for electrons that is somewhat similar to the transport of photons which is known as the *Condensed History Monte Carlo Method*. As with photons, this method breaks the electron energy loss into steps, or path lengths, that combine to describe the electrons complete history. The steps must be chosen such that they are long enough to satisfy the multiple scattering theories, but short enough to ensure that the energy loss is small compared to the kinetic energy of the electron [17]; each step is further divided into substeps to ensure that the

electron trajectory after a major step is accurate. Angular deflections and energy losses at each step can be sampled by the appropriate multiple scattering theory. Data tables are used to sample for bremsstrahlung x-rays, K x-rays and knock-on electrons at each substep. A substep can produce one or no photons, and if one is produced, the energy and direction of the photon is sampled from the tables. The electron trajectory is unaffected by the production of the photon, however, it will lose whatever energy was obtained by the photon at the end of the substep. The production of K x-rays follows the same process as described earlier for photons. Knock-on electrons are only tracked if their energy after collision is greater than 1 keV (low energy cut-off for electrons). Due to the approximations made by the multiple scattering theories, the energy and direction of the primary electron is not updated following the collision.

CHAPTER 3 EXPERIMENTAL AND MODELING METHODOLOGY

3.1 Experimental Apparatus

3.1.1 X-Ray Generator

The general working principle of an x-ray generator is that x-rays are produced through electron impact with some target material. Electrons are emitted from a cathode and collected at an anode, therefore establishing an electron beam through the tube. The cathode and anode are connected to a high voltage power source to accelerate electrons emitted from the cathode and these electrons collide with the anode material, interacting with the material via the same mechanisms discussed in Chapter 2 [26]. Figure 3.1 shows a schematic of a general x-ray tube, and illustrates the x-ray generation process.

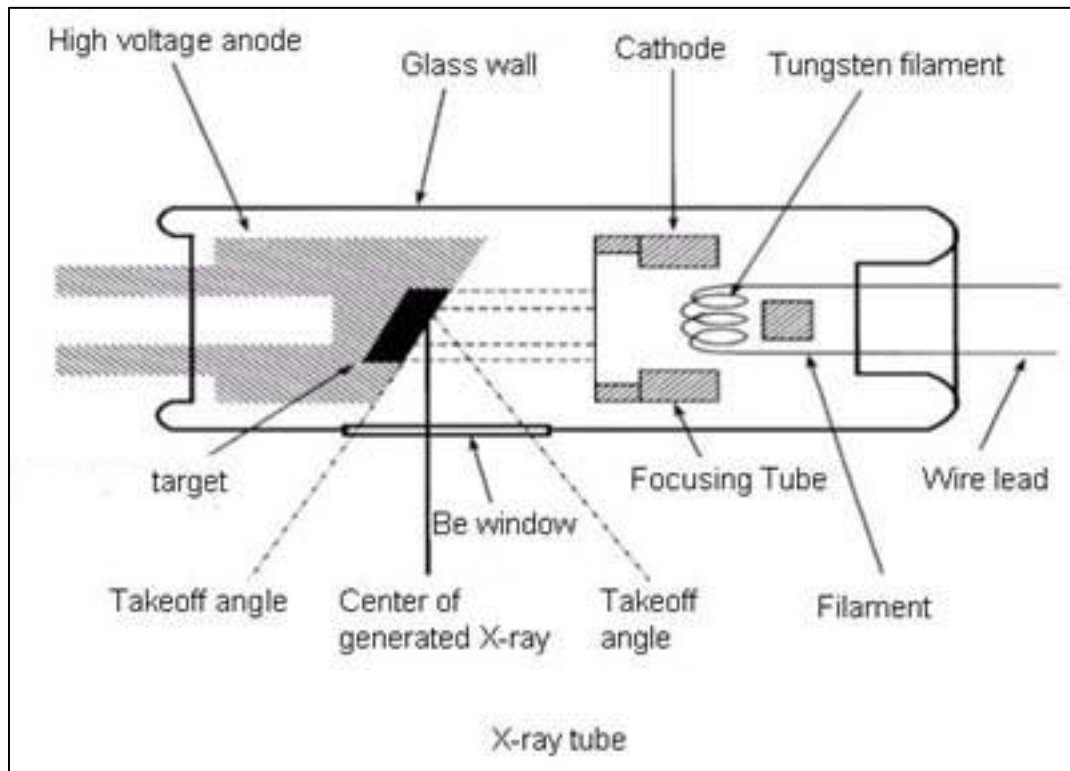


Figure 3.1 X-ray tube schematic [23]

The energy of these electrons is related to the voltage setting, such that, if the voltage is set to 10 kV, then the energy of the electrons will be 10 keV. X-ray production is a very inefficient process, because 99% of the energy released is in the form of heat and many of the low energy x-rays are absorbed in the tubes medium [25]. In fact, less than 1% of the energy released is used to generate Bremsstrahlung and characteristic x-rays. Recall that the energy that an electron loses as it is being slowed down by its Coulomb interaction with an atomic nucleus is given off as Bremsstrahlung x-rays. These x-rays will have a continuous energy spectrum, with a maximum energy equal to the electron energy, and can be produced at almost any voltage setting. Characteristic x-rays are also produced, but recall that their energies are discrete. Furthermore, the production of characteristic x-rays is largely dependent on the energy of the electrons and the material makeup of the target. The intensity of the x-ray beam can be adjusted by changing the applied current. As shown in Figure 3.1, the x-rays are emitted in an output cone from the target; the angle of the cone is generally based on the angle of the target with respect to the electron beam. The output beam can be narrowed through the use of a collimator if the cone is too broad for practical use [26].



Figure 3.2 Mini-X x-ray source

The x-ray generator that was used for this study was the Amptek Miniature Portable X-Ray Tube (Mini-X), illustrated in Figure 3.2 above. The Mini-X is a self-contained x-ray tube system which includes the x-ray tube, power supply, control electronics and USB communication for PC connections. It has a maximum operating voltage of 40 kV and a minimum operating voltage of 10 kV. Also, it has a maximum operating current is 200 μA and a minimum operating current is 5 μA . The Mini-X uses a silver anode for x-ray production and the spectrum at different operating voltages can be seen in Figure 3.3 [27]. As expected, each spectrum has a Bremsstrahlung continuum, and characteristic x-ray energies are only seen for operating voltages greater than 30 kV. These peaks correspond to the K x-rays of silver. It should be noted that these spectra correspond to a filtered x-ray source.

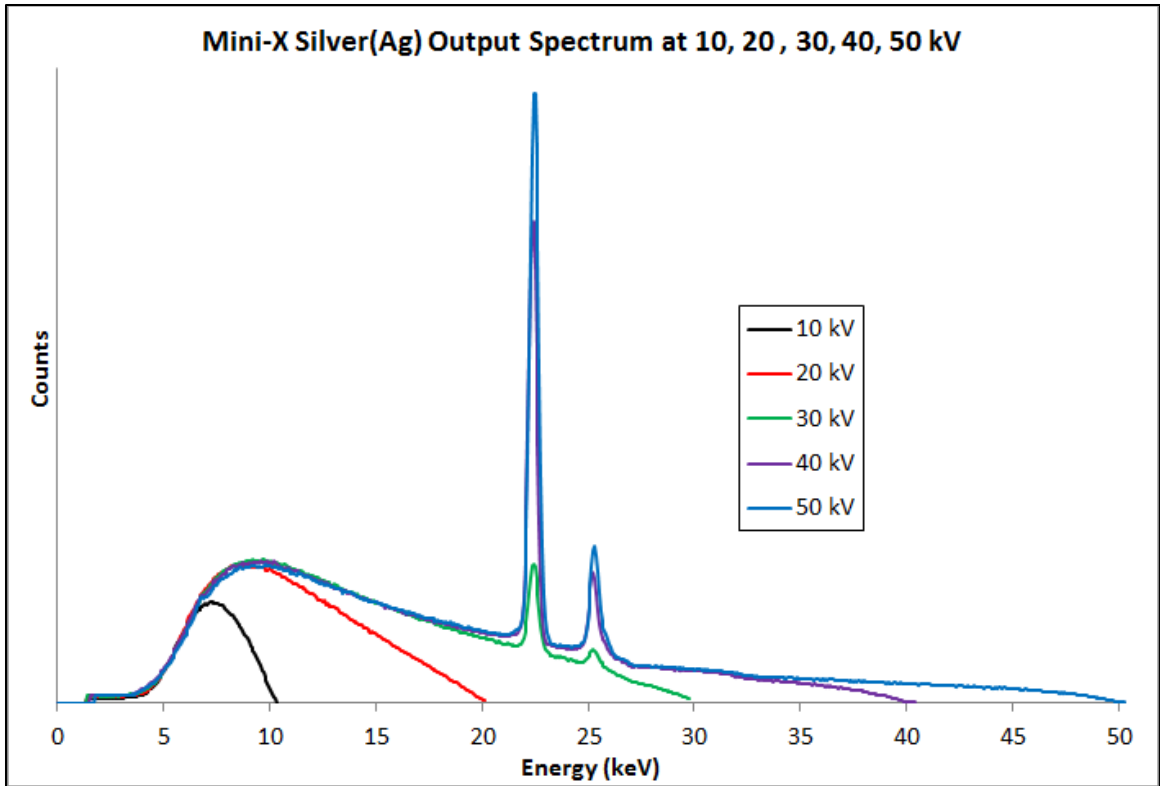


Figure 3.3 Mini-X Output Spectra at various voltages [27]

An attractive feature of the Mini-X is that the spectrum generated at 20 kV is approximately similar to what one would expect from the tritium beta energy spectrum. With this in mind, it is clear that if characteristic x-rays are to be used to modify the Mini-X spectrum, then the target material must be arranged in such a way that the characteristic x-rays it emits are adding to the 20 kVp spectrum and not filtering out too many higher energy photons.



Figure 3.4 Mini-X accessories [27]

Figure 3.4 shows the Mini-X along with some of its accessories. The brass safety plug is meant to be installed when the Mini-X is not in use. If the tube is in operation, the brass plug will reduce the dose rate to less than $25 \mu\text{Sv/h}$ at 5 cm away. When the Mini-X is not collimated, the output cone has an angle of 120° , which is a fairly broad x-ray beam. In order to make the beam narrower, a collimator can be used; for this work, the 2 mm collimator was used. When this collimator is installed, it reduces the angle of the output cone to only 5° [27]. The Mini-X also has a set of filters that fit in the screw-on brass cover. The practical use of filters is illustrated in Figure 3.5. In general, filters are useful because they can absorb low energy x-rays well, and they can significantly reduce the x-ray intensity. However, the use of filters can pose some issues and this will be explored in the next chapter.

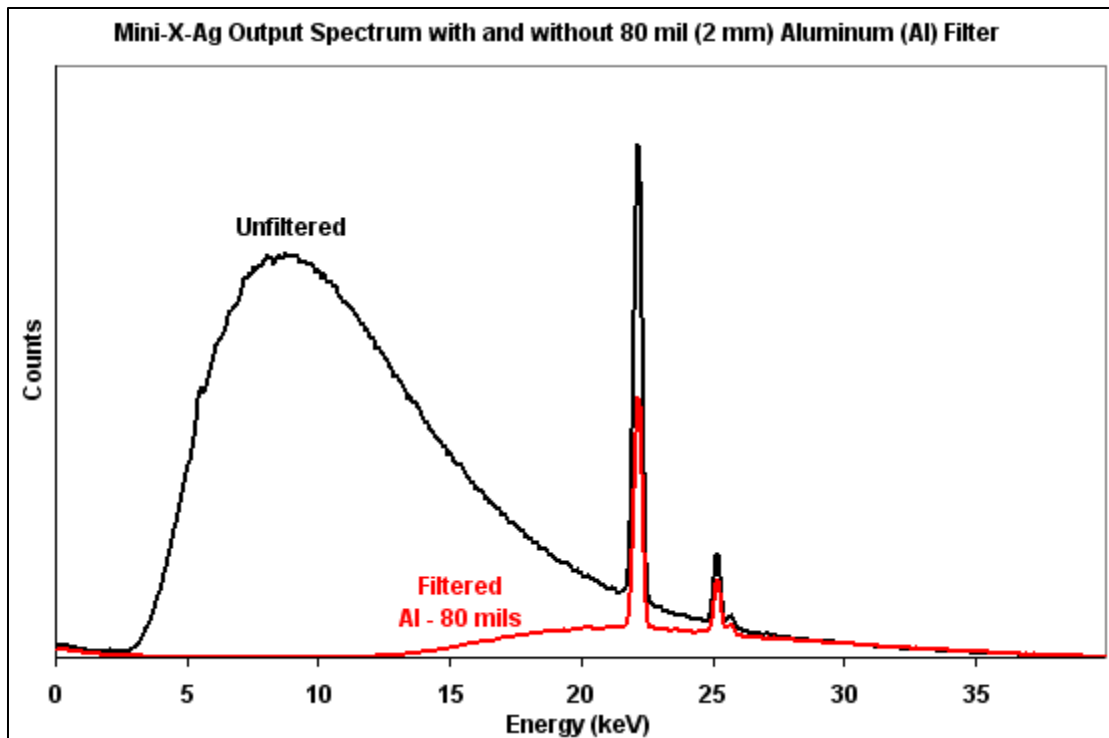


Figure 3.5 Comparison of filtered and unfiltered spectra [30]

3.1.2 X-Ray Detector

For this thesis, a *silicon drift detector* (SDD) was used for x-ray detection. This detector is a solid state detector that measures the energy of a photon by the amount of ionization it produces in the detector material, which is high purity silicon [28]. The advantages of SDDs are listed as follows [29]:

- Can measure higher count rates than other x-ray detectors
- High energy resolution (ie. 125 eV FWHM at 5.9 keV)
- Can eliminate edge effects and false peaks
- High peak-to-background ratio
- Do not require liquid nitrogen for cooling

The detector that was used for this study was the Amptek X-123 Silicon Drift Detector (X-123), shown in Figure 3.6.



Figure 3.6 X-123 x-ray detector

This spectrometer includes the SDD, preamplifier, digital pulse processor (DPP), multichannel analyzer (MCA) and a power supply. As with the Mini-X, the X-123 has a USB connection for communication with a computer. The SDD is mounted on a thermoelectric cooler and coupled to a custom charge sensitive preamplifier; the cooler in particular reduces the electronic noise in both the detector and preamplifier. The DPP digitizes the preamplifier output, applies real-time digital processing to the signal, detects the peak amplitude and bins this in its histogram memory [29]. The spectrum is then transmitted to the data acquisition software; the software interface can be seen in Figure 3.7. This software also allows the user to adjust the settings and control the operation of the detector. Before experimental data was to be taken, the detector was calibrated using an iron-55 source. Iron-55 is a radioactive isotope with a half-life of 2.737 years. It decays via electron capture, and emits x-rays with energies 5.89 keV and 6.49 keV.

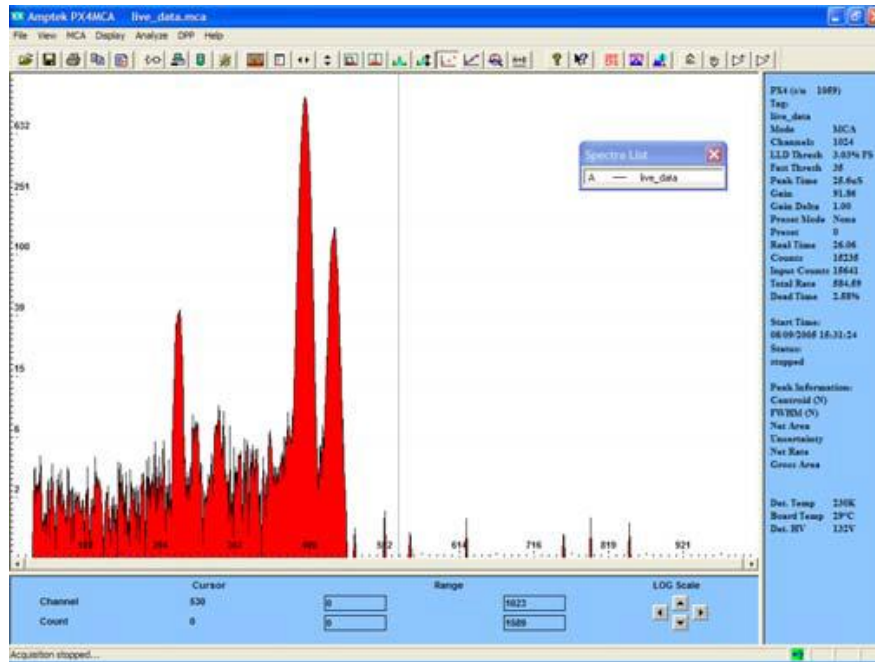


Figure 3.7 Data acquisition software [29]

3.1.3 Target Materials

The target materials that were chosen to investigate the production of characteristic x-rays were iron and titanium, which are shown in Figure 3.8. Also shown in this figure is germanium, but this target was not used for investigation.

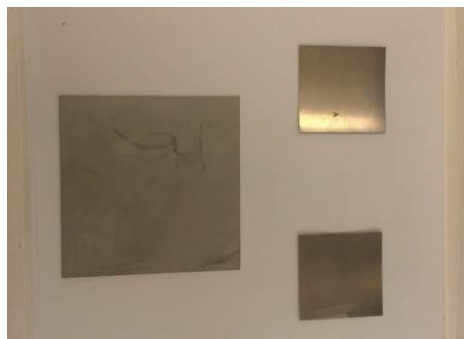


Figure 3.8 Target materials; Germanium (left), Titanium (top right) and Iron (bottom right)

Iron and titanium were chosen because of their K x-ray energies, which lie in the region where the Mini-X spectrum is less intense. Table 3.1 shows the K x-ray energies, thickness and fluorescent yield for both materials. L x-rays have a very low yield for these materials (~0.1%), so they were not considered.

	Iron	Titanium
K_{α} (keV)	6.403	4.510
K_{β} (keV)	7.057	4.931
Thickness (μm)	75	100
Fluorescent Yield	0.340	0.214

Table 3.1 Characteristic x-ray energies, thickness and yield for materials [31]

3.1.4 Experimental Setup

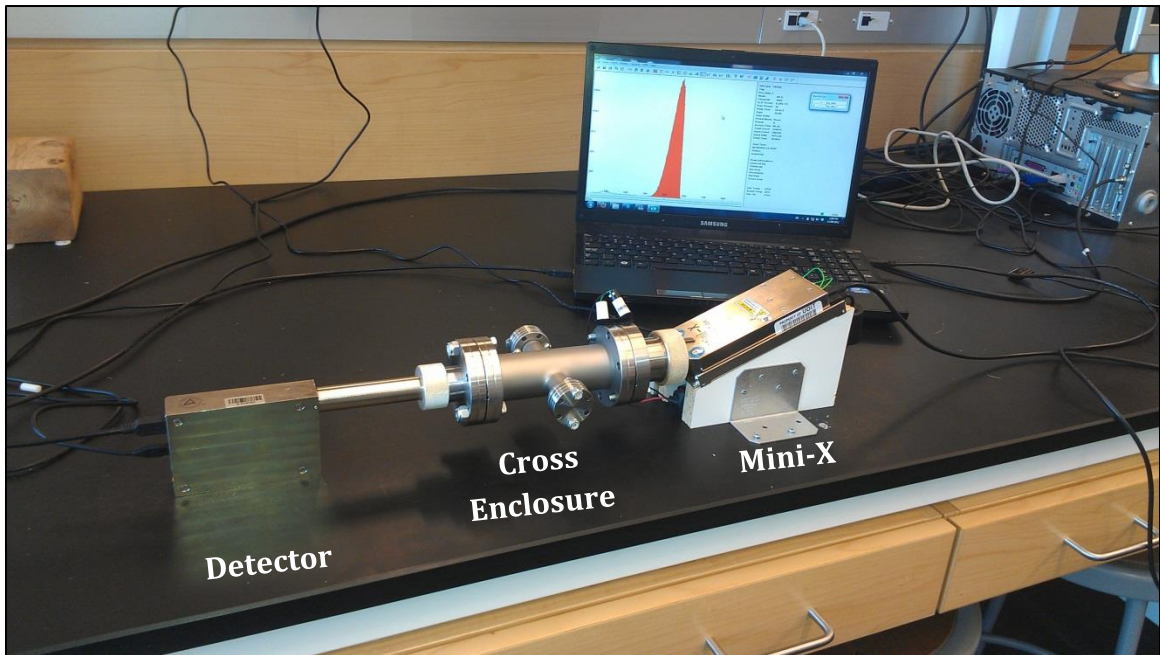


Figure 3.9 Experimental setup

The experimental setup is shown in Figure 3.9. The Ontario Ministry of Occupational Health and Safety regulations require that any x-ray device to be used in a permanent location must be fixed in place, so the Mini-X is mounted on two

pieces of wood and fixed to the workbench in the lab. Also in Figure 3.9 is the 'cross' enclosure which has two purposes. The first is that it allows the Mini-X and detector to be coupled, such that they are along the same axis. Secondly, the cross acts as a radiation shield, capable of preventing 40 keV x-rays from escaping the enclosure. Not shown in Figure 3.9 is the target material, which is inside the enclosure, directly in front of the Mini-X.



Figure 3.10 Mini-X's interlock and LED [27]

There are also safety features in place to prevent accidental exposure to the user. One feature is the Mini-X's alarm, which sounds off a series of beeps and flashes an LED while the Mini-X is in use. The LED can be seen in Figure 3.10 at the J3 label. Also shown in the figure is the second feature, the Mini-X's hardware interlock. For the Mini-X to be used, pins 1 and 2 on the interlock must be connected together. If the connection is broken while the Mini-X is producing x-rays, the Mini-X will be disabled and the user will have to re-establish the connection and restart it. The user has the option of interfacing an external safety mechanism with the interlock for added security, which has been done by implementing a circuit with the interlock. Figure 3.11 shows a schematic of the circuit.

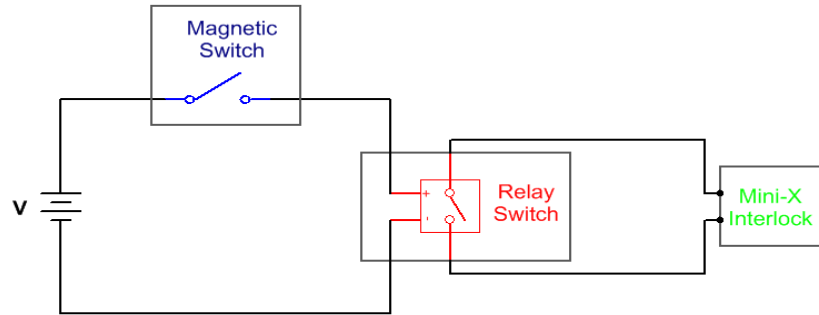


Figure 3.11 Schematic of circuit that controls interlock

This circuit uses a magnetic switch which is mounted on the cross enclosure and the Mini-X's conflat (see Figure 3.9). When the conflat and the cross are in contact, the interlock connection is closed and the Mini-X can be used. When the two are not in contact, the interlock connection is opened, preventing the Mini-X from producing x-rays, and ensuring no accidental exposure to the user. For more information regarding the experimental setup, see Appendix B.

3.2 Modeling Methodology

Computational modeling was used to investigate many aspects of this thesis. Models were developed to simulate characteristic x-ray production from an iron target, titanium target and a composite iron-titanium target. Also, another model was developed to investigate the electron spectrum generated in water. In most cases, the photon source was modeled to simulate the Mini-X at a 20 kV operating voltage, however some characteristic x-ray simulations used a monoenergetic beam at different energies. The models for the characteristic x-ray simulations all had the same basic input file, with minor differences, such as target composition and thickness. A generic input file for these simulations can be found in Appendix C.

Figure 3.12 illustrates the basic geometry for the models; for these simulations, the green object would correspond to the target material, and the blue object to the 'detector'. This figure was generated with the MCNP Visual Editor software called VISEDX [17].

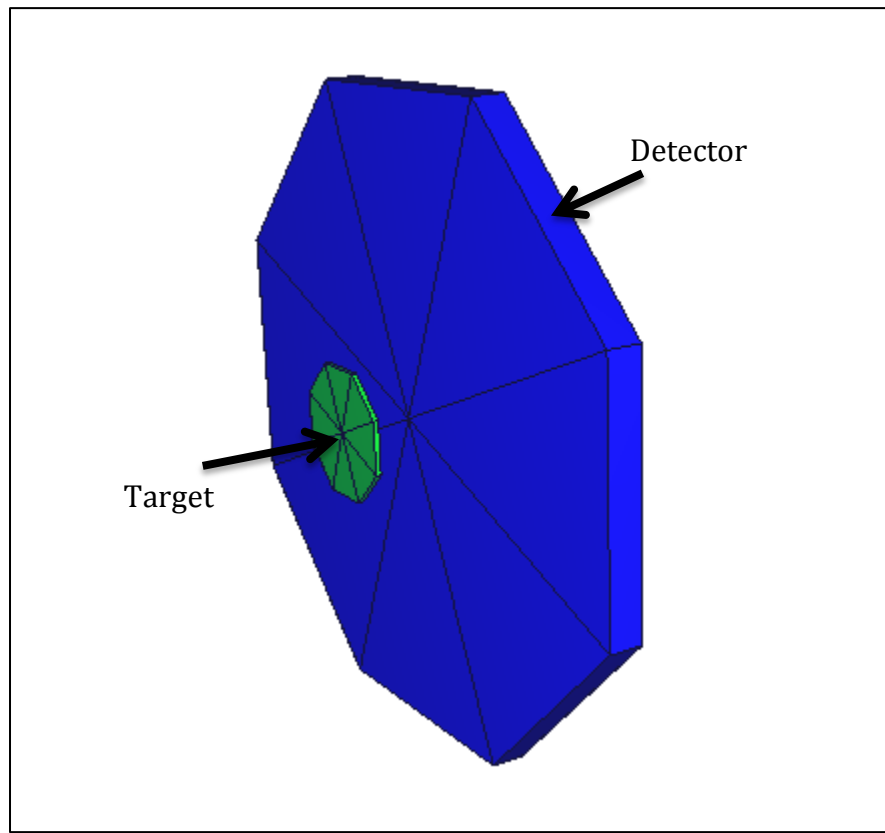


Figure 3.12 Illustration of characteristic x-ray model

Not seen in Figure 3.12 is the photon source, which was modeled as a circular, planar source, with a circumference equal to that of the target. Also, the source was situated in front of the target, such that all emitted photons would cross its boundary surface. The detector area was chosen to be much larger than the target, in order to measure as many characteristic x-rays emitted in the forward direction (away from the source) as possible. The target was modeled based on the

thicknesses and expected irradiated area of iron and titanium. For the composite target simulations, a thickness of 75 μm was used.

The geometrical model that was developed to investigate the electron spectrum in water was similar to the one seen in Figure 3.12, with the detector being replaced by a slab of water, and the target was an aluminium absorber. Water slabs of varying thicknesses were used. The photon source was modeled to simulate an unfiltered Mini-X output spectrum. The MCNP input file for this model can be seen in Appendix C.

CHAPTER 4 RESULTS AND DISCUSSION

4.1 Theoretical Predictions

The early work for this research first sought to determine the amount of K shell ionizations that would result in the emission of a characteristic x-ray (as opposed to an Auger electron emission), and how many will escape the target in the forward direction (see Figure 1.3). A prediction for characteristic x-ray production within the target can be determined by taking into account the interaction rate of source photons within the target material. From the interaction rate, the following equation for the fluorescence rate, F , is given as [32]:

$$F = \phi \mu_{mp} \rho V \omega \quad 4.1$$

Where ϕ is the photon flux, μ_{mp} is the mass photoionization attenuation coefficient, ρ is the density, V is the volume and ω is the fluorescent yield of the target material. This equation describes the rate at which characteristic x-rays are being produced in the target. Without the fluorescent yield parameter, this formula is similar to the one used to determine the photon interaction rate within a target [32]. It should be noted that the volume and flux in Equation 4.1 will depend on the distance, d , between the source and the target, due to the Mini-X's output cone, as shown in Figure 4.1.

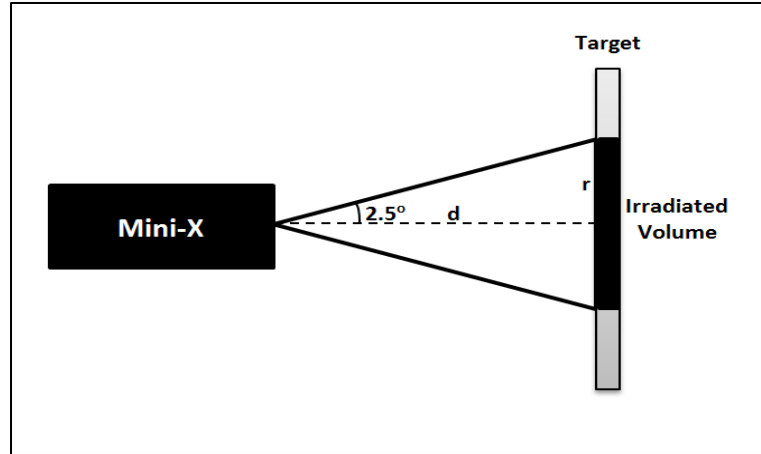


Figure 4.1 Illustration of Mini-X irradiation area

The Mini-X has a 5° output cone, and at any distance, the source will irradiate a thin cylindrical volume with radius r and thickness t . For the purpose of this research, the distance between the source and target is no more than 1 cm. At this distance however, all source photons will be incident on the target; therefore, moving the target closer to the source will change both the flux and irradiated volume proportionally, resulting in the same fluorescence rate.

Recall that the materials used for this thesis were iron and titanium, which have thicknesses of 75 μm and 100 μm respectively. Table 4.1 shows some additional physical data for both materials that were used for fluorescence rate calculations. Lastly, a flux of $10^6 \text{ cm}^{-2}\text{s}^{-1}$ was used for all energies since this is approximately the same flux emitted from the Mini-X.

Data for Iron and Titanium		
	Iron	Titanium
ω	0.340	0.219
$M \text{ (g/mol)}$	55.85	47.90
$\rho \text{ (g/cm}^3\text{)}$	7.860	4.506
$V \text{ (cm}^3\text{)}$	4.49156×10^{-5}	5.9887×10^{-5}

Table 4.1 Physical data for target materials [31]

Fluorescence Rates for Iron		
Energy (keV)	μ_m (cm^2/g)	Rate (s^{-1})
7.112*	405.9	48721
8	304.0	36490
9	224.3	26923
10	169.4	20333
15	56.23	6749
20	25.05	3007

Table 4.2a Calculated Fluorescent Rates for iron

*Binding energy

Fluorescence Rates for Titanium		
Energy (keV)	μ_m (cm^2/g)	Rate (s^{-1})
4.966*	685.9	39609
5	682.0	39384
6	430.8	24878
8	201.1	11613
10	109.7	6335
15	35.18	2032
20	15.33	885

Table 4.2b Calculated Fluorescent Rates for titanium

*Binding Energy

For k-shell ionizations, the binding energy for iron and titanium is 7.112 keV and 4.966 keV respectively [31], so only energies greater than these were considered for each material. Tables 4.2a and 4.2b display the results for the fluorescence rate calculations, up to a maximum energy of 20 keV. From these calculations, the most notable trend is that the fluorescence rate decreases with increasing energy. This is expected since the rate is directly proportional to the cross section, which also decreases with increasing energy. Another observation is that iron is more fluorescent than titanium at a similar energy. This result confirms the trend seen in Figure 2.7, where the fluorescent yield was seen to increase with increasing atomic number. This result will have some important consequences as will be seen later.

The overall fluorescence rates for both materials appear to be producing an adequate amount of characteristic x-rays per second. What remains to be seen, however, is how many of these x-rays will be emitted in the forward direction, and of those, how many will escape the target. Predicting this analytically is challenging, since it largely depends on where the source photon interacts within the material and the emission direction of the characteristic x-rays, which are both stochastic processes. In light of this, MCNP was used.

For these simulations, 10^7 starting particles were used, and photons arriving at the detector were tallied. MCNP output files also indicate the number of characteristic x-rays that were produced. The results are shown in Tables 4.3a and 4.3b. In these tables, the K x-ray rows are the number of characteristic x-rays arriving at the detector, and the Fluorescence row indicates the number of interactions that resulted in the emission of a characteristic x-ray (as opposed to an Auger emission).

Simulation Results for Iron					
	5 keV	8 keV	10 keV	15 keV	20 keV
K_α (6.40 keV)	0	151	177	1087	1825
K_β (7.06 keV)	0	59	65	217	289
Fluorescence	0	85780	85751	82714	66401

Table 4.3a Simulation results for iron

Simulation Results for Titanium					
	5 keV	8 keV	10 keV	15 keV	20 keV
K_α (4.51 keV)	22	38	137	540	518
K_β (4.93 keV)	12	8	25	91	92
Fluorescence	32056	32036	31780	25642	16040

Table 4.3b Simulation results for titanium

At 5 keV for iron, no fluorescence events occur in the material, which is expected since a 5 keV photon has insufficient energy to liberate a K shell electron in iron. In general, the trend seen from the simulation results is that the number of characteristic x-rays arriving at the detector increases with increasing energy. The reason for this is because higher energy photons are more likely to have interactions deeper within the target, which in turn gives the characteristic x-rays a better chance of escaping the remaining target material in the forward direction. This also explains why the simulation for 20 keV photons incident on titanium tallied less characteristic x-rays at the detector than the 15 keV case. To see why, recall Equation 2.1b:

$$P = e^{-\mu_m \rho t} \quad 4.2$$

Where t is the thickness of the target material. At 15 keV and 20 keV, there is a 20% chance and a 49% chance, respectively, that a photon can pass through the titanium target. Compare this with iron, where at 20 keV, a photon only has a 22% chance of escaping. Therefore, since fewer photons are interacting with titanium at 20 keV, there is less characteristic x-ray production.

From the results, it may be seen that many of the characteristic x-rays that were produced in the target were not detected. At 20 keV in particular, only 2.7% and 3.2% of the characteristic x-rays produced were detected for iron and titanium respectively; the percentages are even less for the lower energy simulations. These losses can be attributed to two main reasons. The first is that characteristic x-rays

are emitted isotropically, so the emission distribution is spherical. This implies that there will be geometric losses that depend on the distance between the target and the detector, and the detectors area. An approximation for these losses can be determined by calculating what is known as the geometric efficiency [28], which is a quantity that takes into account the fact that only a fraction of the emitted x-rays will be detected. The second reason for the losses seen is due to the fact that characteristic x-rays can be absorbed (attenuated) in the target material.

4.2 Characteristic X-Ray Simulation Results

4.2.1 Composite Target

Characteristic x-rays are commonly used for elemental analysis due to the unique energies emitted by each atom, through a process called X-Ray Fluorescence (XRF) Spectroscopy [33]. From these analyses, it has been found that the composition of a given material is essentially proportional to the relative intensity of the K x-rays measured. The results from the last section confirmed that iron is more fluorescent than titanium. However, in order to mimic the beta decay spectrum of tritium accurately, titanium must yield a greater intensity than iron. Based on the results of XRF analysis, this implies that if a composite target is to be constructed, the target composition must have more titanium than iron. To determine the composition needed, simulations were done to analyse the characteristic x-ray output for a composite target of differing compositions of iron and titanium. These simulations used a 15 keV photon source, and characteristic x-rays were tallied in the silicon detector, but only the K_{α} x-ray counts were

considered. The composition for each simulation was specified by atom fractions, and a target thickness of 75 μm was used. Seven simulations were performed, the results of which can be seen in Figures 4.2a-4.2g. Note that the iron K_{α} counts are at 6.4 keV, and the titanium K_{α} counts are at 4.51 keV.

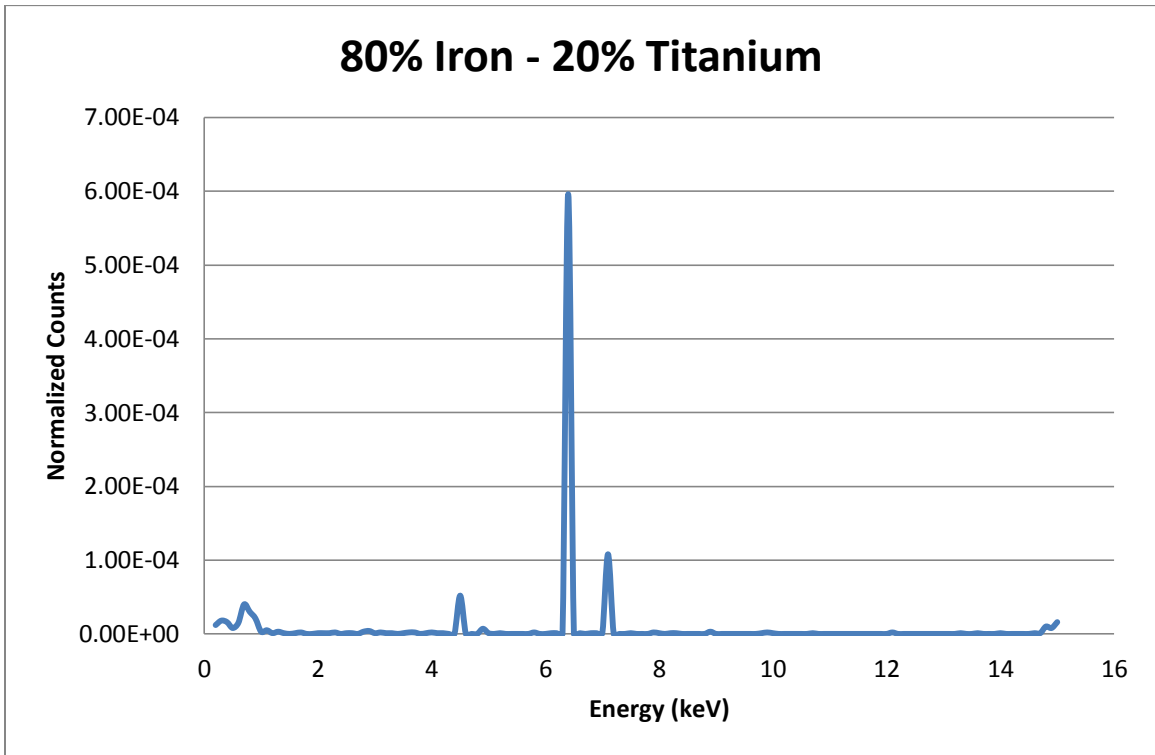


Figure 4.2a X-ray spectra for composition of 80% iron, 20% titanium

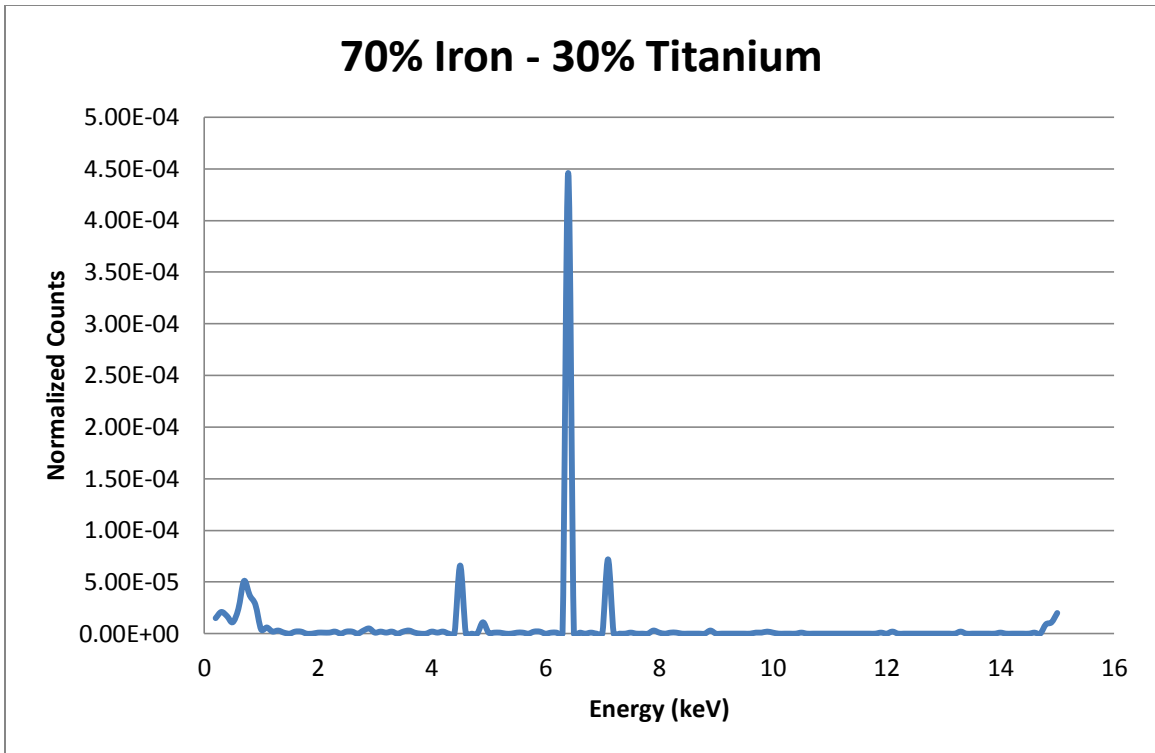


Figure 4.2b X-ray spectra for composition of 70% iron, 30% titanium

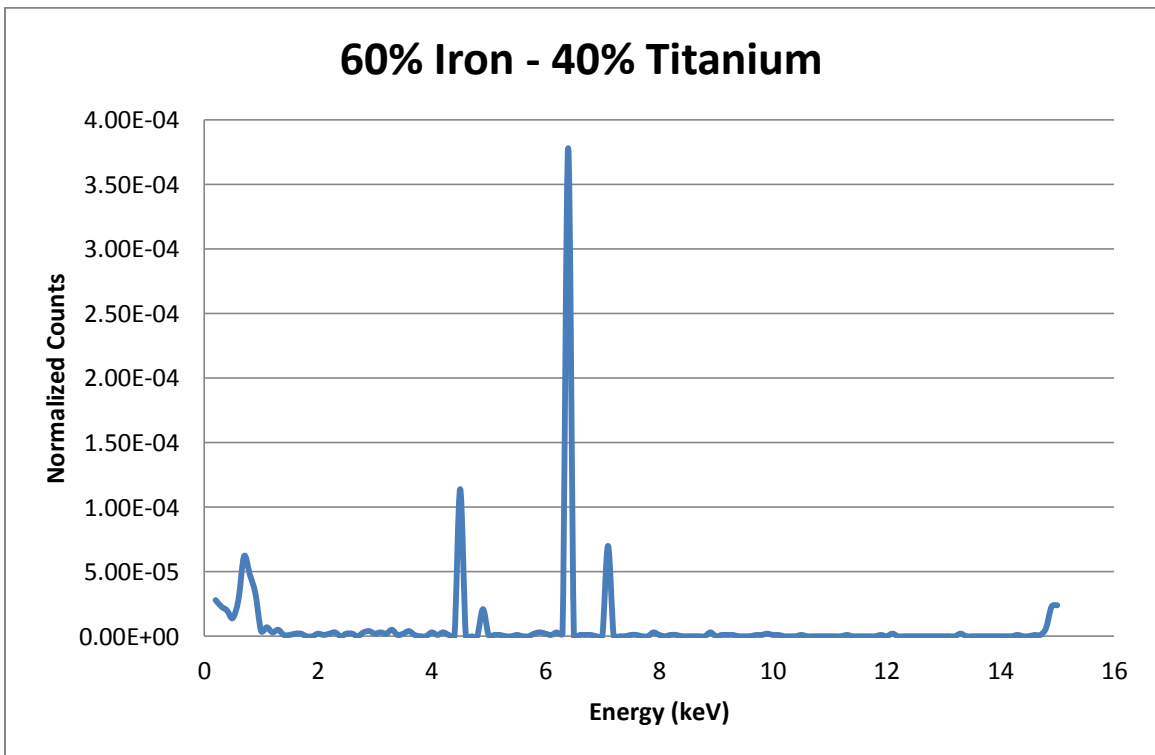


Figure 4.2c X-ray spectra for composition of 60% iron, 40% titanium

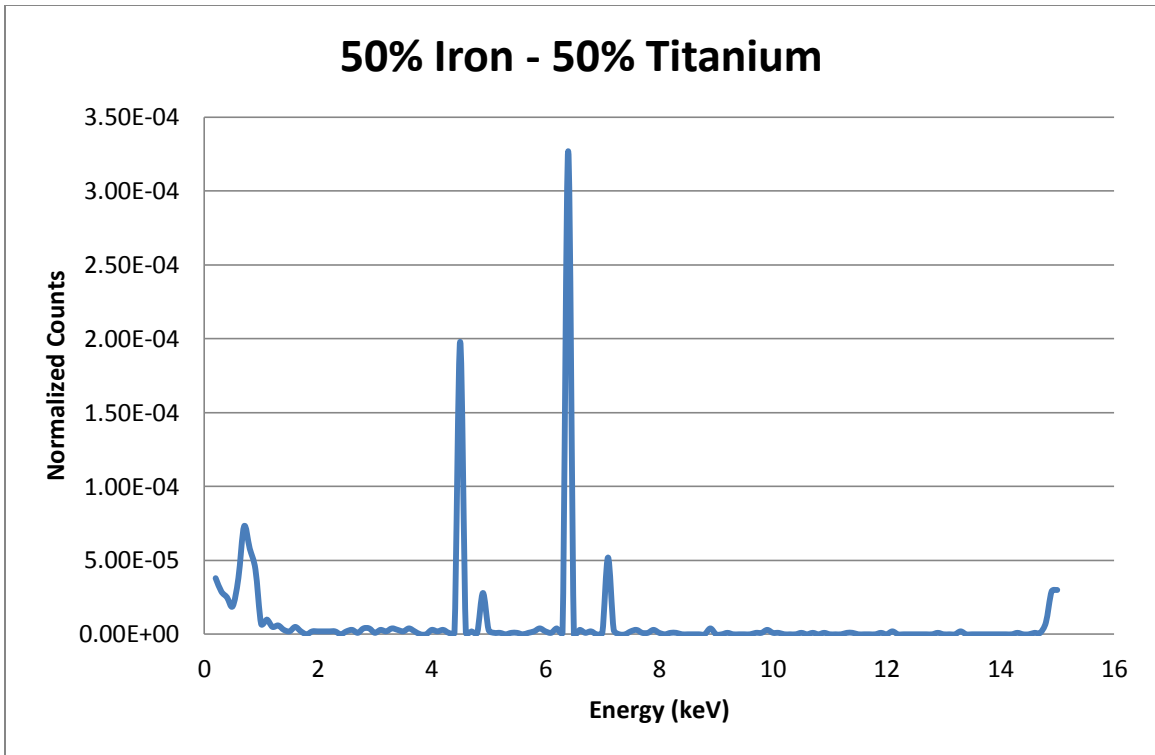


Figure 4.2d X-ray spectra for composition of 50% iron, 50% titanium

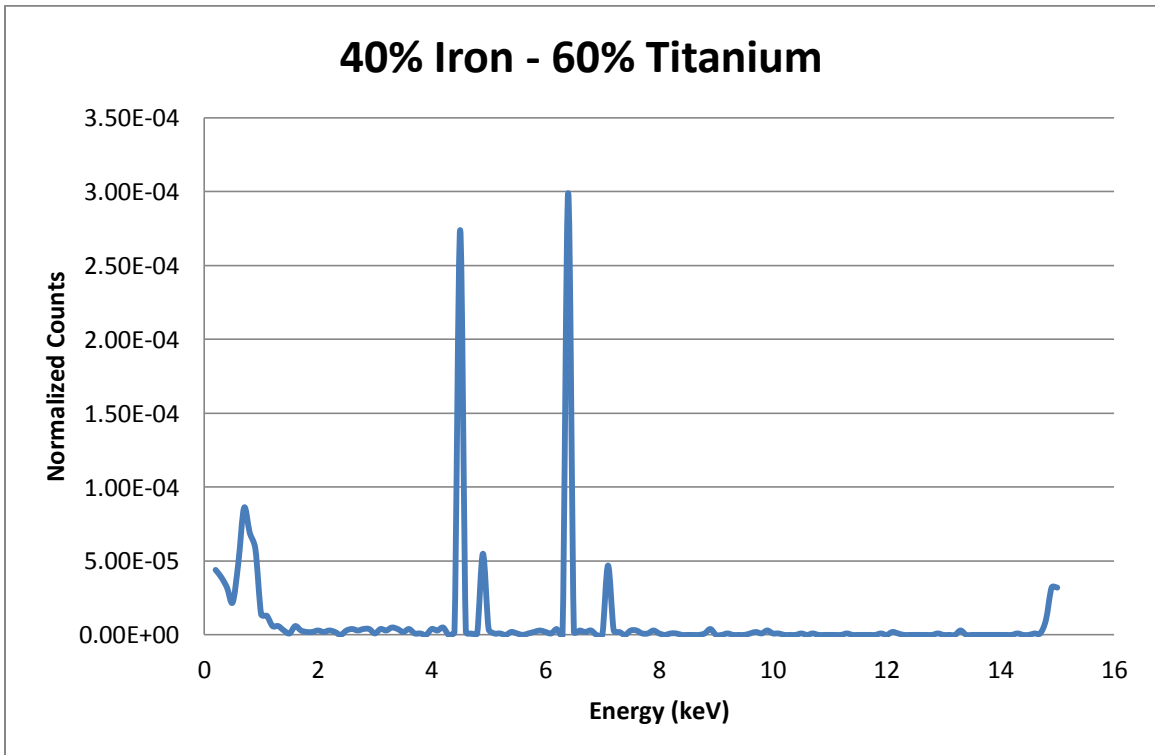


Figure 4.2e X-ray spectra for composition of 40% iron, 60% titanium

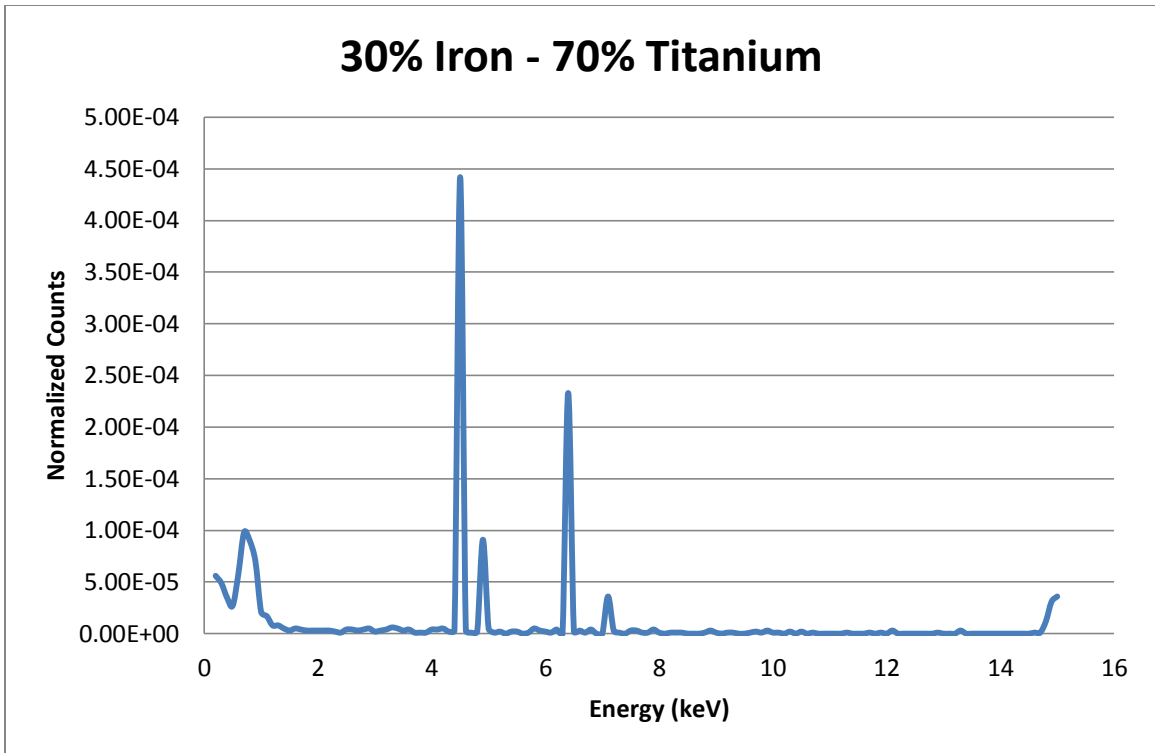


Figure 4.2f X-ray spectra for composition of 30% iron, 70% titanium

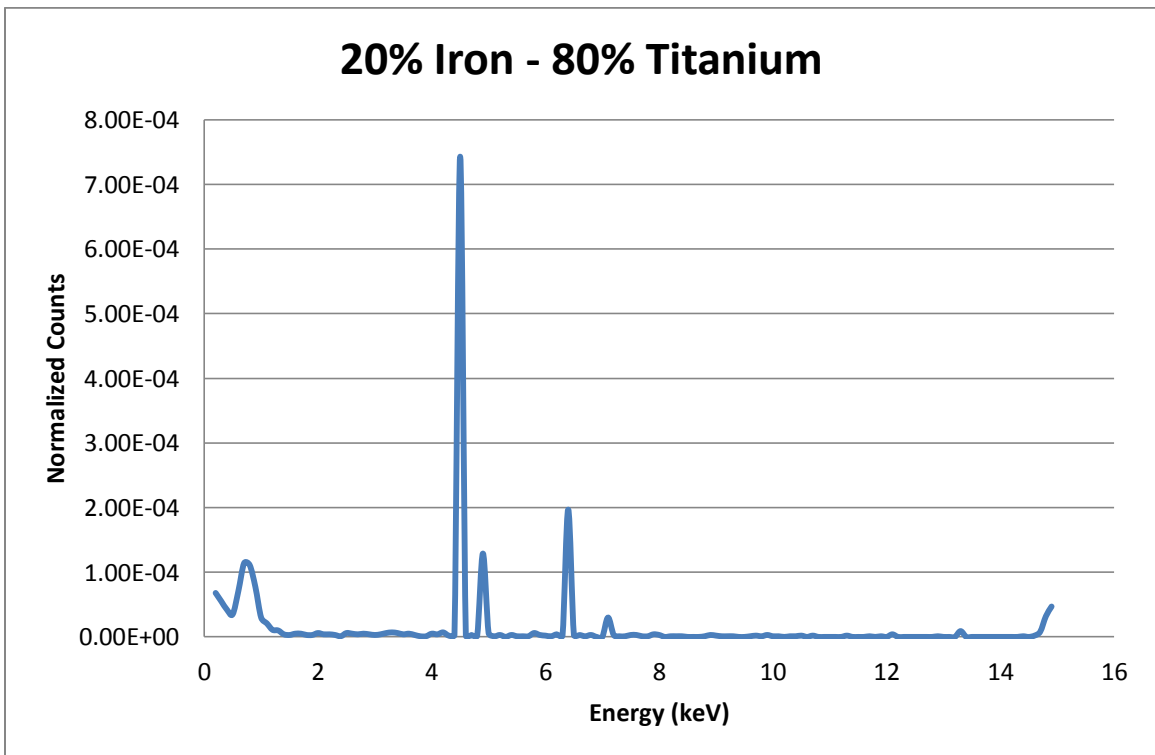


Figure 4.2g X-ray spectra for composition of 20% iron, 80% titanium

The Figures show how varying the material composition affects the relative intensity of the K x-rays. Table 4.4 shows the ratio of normalized K_{α} counts for titanium, C_{Ti} , and iron, C_{Fe} , for different atom fractions of titanium.

Titanium Atom Fraction	C_{Ti} ($\times 10^{-5}$)	C_{Fe} ($\times 10^{-5}$)	Ratio (C_{Ti}/C_{Fe})
0.2	5.20	59.6	0.08725
0.3	6.60	44.6	0.14798
0.4	11.4	37.8	0.30159
0.5	19.8	32.7	0.6055
0.6	27.4	29.9	0.91639
0.7	44.2	23.3	1.897
0.8	74.3	19.4	3.8299

Table 4.4 Simulation results for composite target

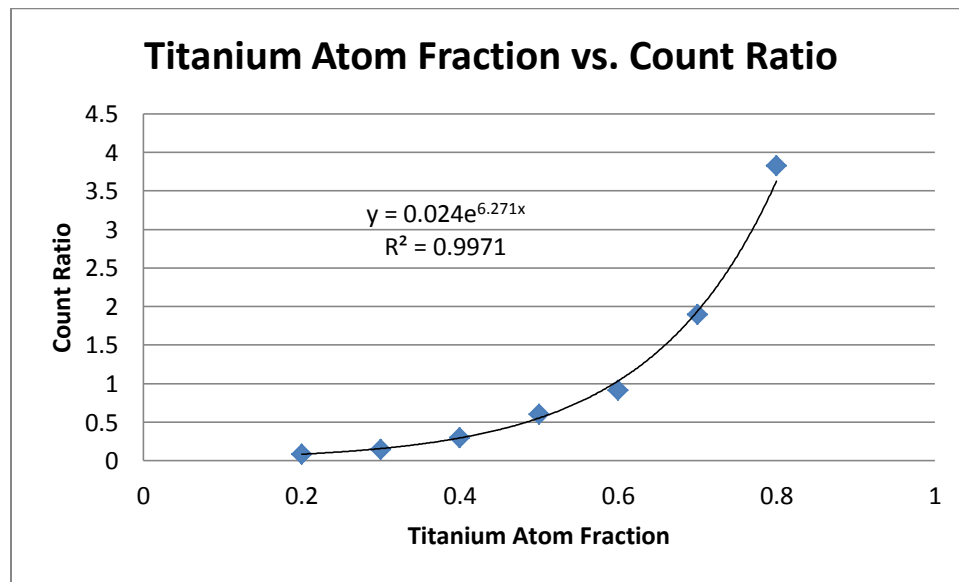


Figure 4.3 Plot of titanium atom fraction versus count ratio

Figure 4.3 shows that the count ratio increases exponentially as the atom fraction of titanium is increased. This exponential relationship arises from the fact that as the atom fraction of titanium is increased, the attenuation coefficient for the composite target decreases. From Equation 2.1b, it is clear that a decreasing attenuation

coefficient allows the primary photons to interact deeper within the target, giving the characteristic x-rays a higher probability of escaping towards the detector. Since the probability of escape is an exponential relation, it is expected that the counts arriving at the detector will also follow an exponential trend. The trendline shown in Figure 4.3 was obtained through regression techniques in EXCEL; the equation for this trendline can be rewritten as:

$$C_R = 0.024e^{6.271A_T} \quad 4.3$$

Where C_R is the count ratio, and A_T is the titanium atom fraction. With this equation, an approximate composition can be predicted that will be suitable for mimicking the tritium beta decay energy spectrum. Recall that the K_α energies for iron and titanium are 6.4 keV and 4.51 keV respectively. The decay spectrum data for tritium is shown in Appendix A, and from this it is seen that at 6.5 keV, the normalized count is 0.01577, and at 4.5keV, it is 0.01869. Since these energies are comparable to the K_α x-ray energies, this indicates that in order to mimic the tritium spectrum, the count ratio for titanium and iron must be:

$$C_R = \frac{C_{Ti}}{C_{Fe}} \approx \frac{C_{4.5}}{C_{6.5}} = \frac{0.01869}{0.01577} = 1.185$$

Rearranging Equation 4.3 to solve for A_T and using the above count ratio gives:

$$A_T = \frac{\ln\left(\frac{C_R}{0.024}\right)}{6.271} = 0.622$$

Therefore, to mimic the tritium spectrum, the composite target must have an atom fraction of 0.622 for titanium, from which it follows that the atom fraction for iron should be 0.378.

4.2.2 Mini-X Simulations

Simulations were performed to model the actual experimental conditions using a photon source that was similar to the Mini-X's output spectrum at an operating voltage of 20 kV_p⁷, and can be seen in Figure 4.4. Simulations were done with an iron target, titanium target, and a composite target with the same atom fractions that were found in the previous section. A thickness of 75 μm was used for the iron and the composite target, and 100 μm was used for titanium.

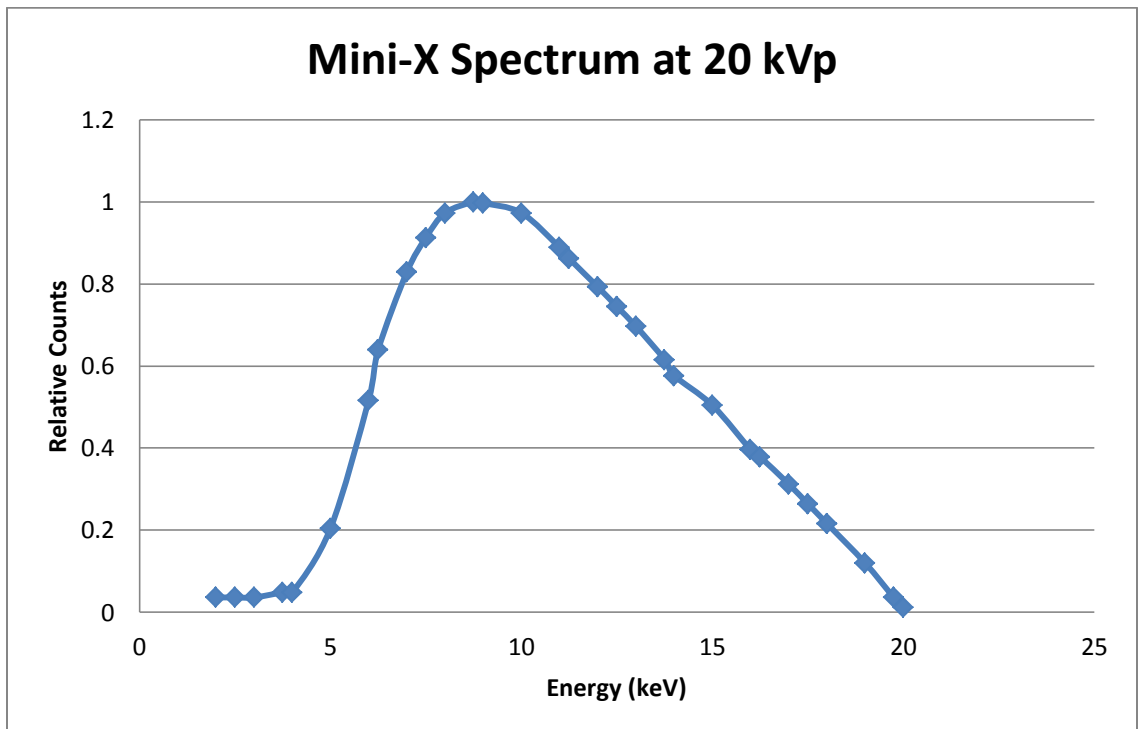


Figure 4.4 Approximate Mini-X output spectrum at 20 kV_p

⁷ See Figure 3.3 for Mini-X output spectrum at 20 kV_p

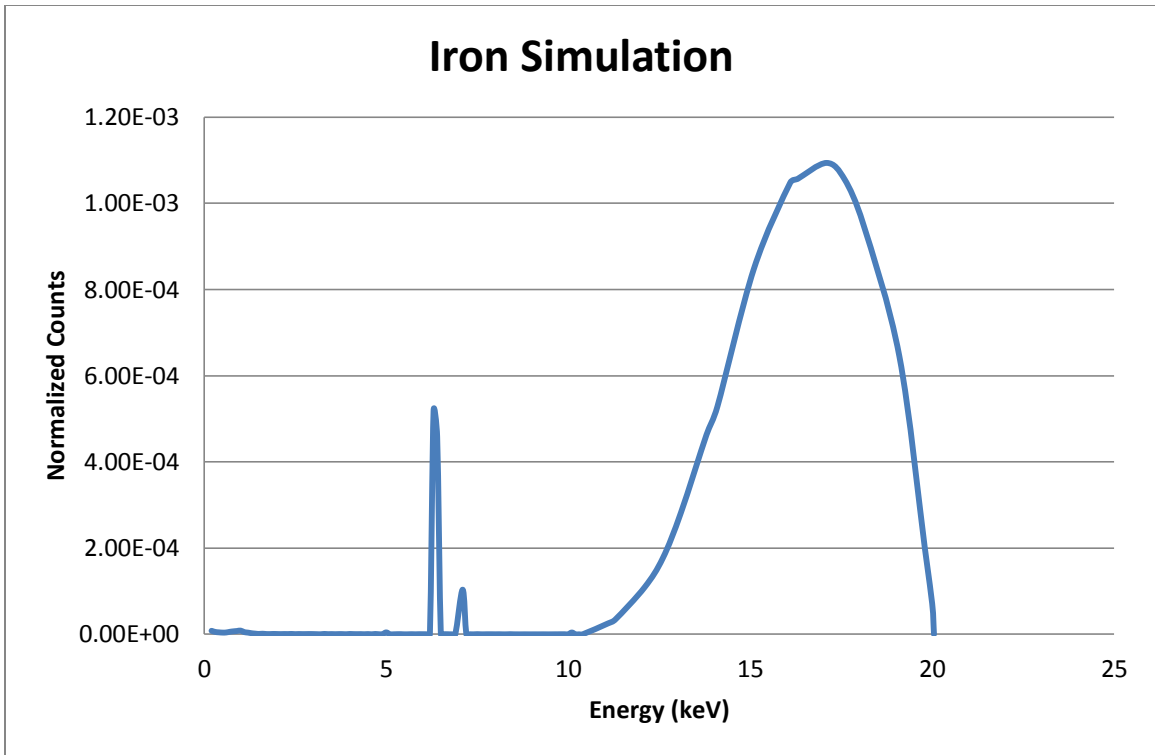


Figure 4.5 Simulation x-ray spectra for iron

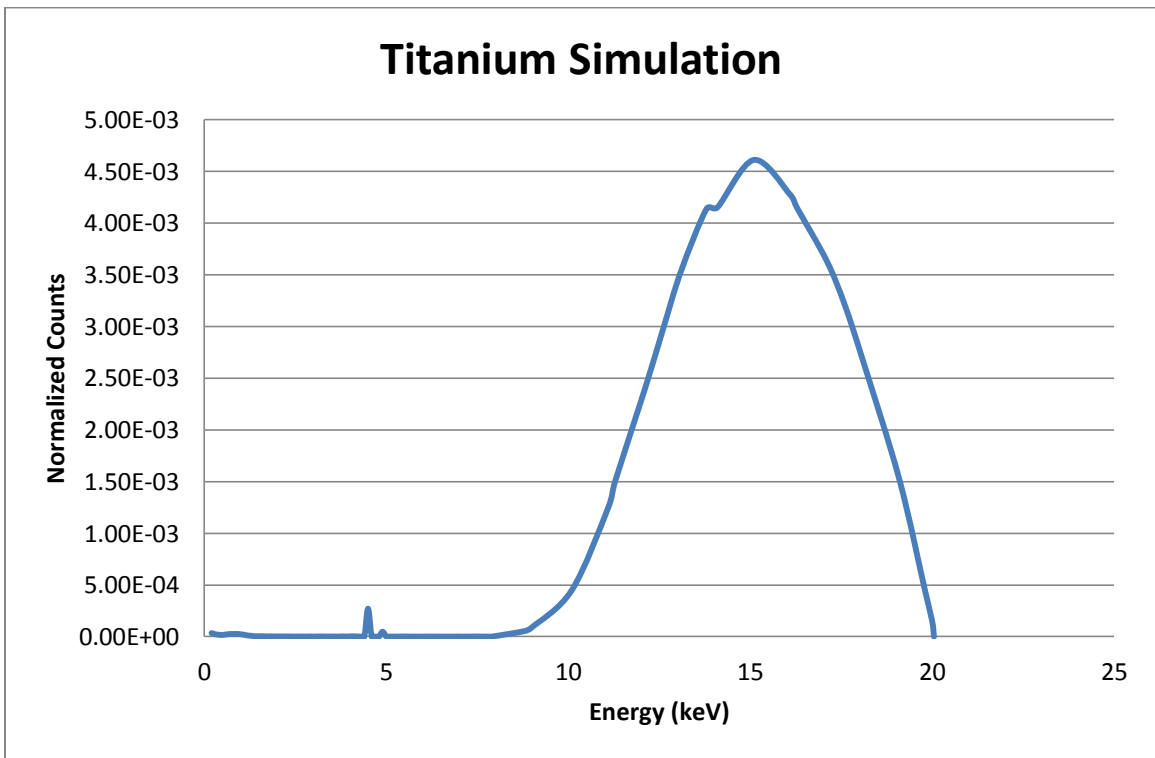


Figure 4.6 Simulation x-ray spectra for titanium

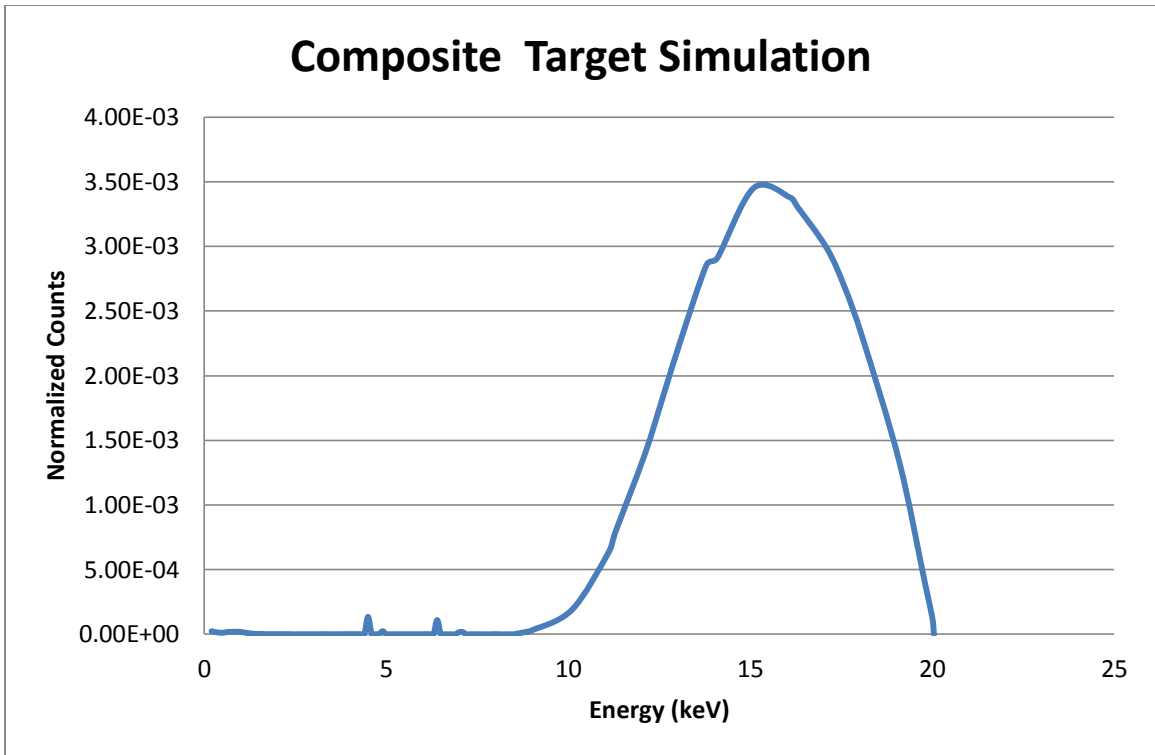


Figure 4.7a Simulation x-ray spectra for composite target

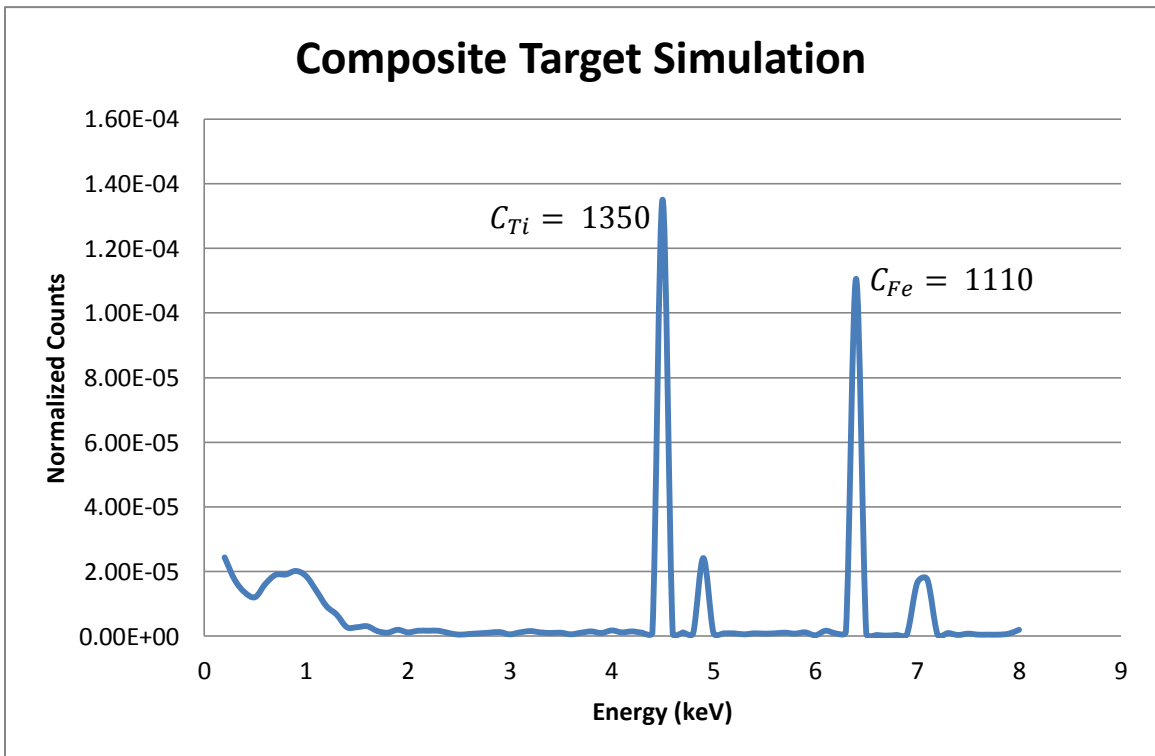


Figure 4.7b Simulation x-ray spectra for composite target (close up)

For both iron (Figure 4.5) and titanium (Figure 4.6), iron is seen to be more fluorescent than titanium. The more noticeable feature from the plots is that many more source photons are being detected than characteristic x-rays; this indicates that there may not be enough characteristic x-rays getting to the detector to meaningfully modify the Mini-X spectrum. This is further demonstrated in Figure 4.7, where the resultant characteristic x-ray peaks from the composite target material are very small. The conclusion to draw from these simulations is that utilizing characteristic x-rays may not be feasible for mimicking the tritium decay spectrum.

4.3 Detector Analysis

Experimental work began with investigating the operation of the Mini-X and the detector. Due to its high count rate ($\sim 10^8$ counts per second at 2cm from source), the Mini-X posed some challenges initially when it came to detecting x-rays. Therefore, the first objective for the experimental work was to determine what detector settings and configurations would resolve the issue of high count rates.

The dead time, τ_d , of a detector is defined as the minimum amount of time that must separate two events in order for them to be recorded as separate pulses [28]. This implies that when count rates are too high, the detector is unable to register all photons interacting with it, which will lead to many losses in photon measurement. Fortunately, the X-123's software allows the user to adjust the dead time by changing the peaking time, τ_p , which is the time required for the shaped

pulse to reach its maximum amplitude [28]. For the X-123, the dead time is related to the peaking time by [29]:

$$\tau_d = 1.05 * \tau_p \quad 4.4$$

The software has up to 24 peaking times, ranging from 0.8 μ s to 102.4 μ s that can be set by the user. From Equation 4.4, the dead time is seen to be proportional to the peaking time, so a longer peaking time corresponds to a lower count rate, and a shorter one corresponds to a higher count rate. With this in mind, a short peaking time would be more suitable for measuring the Mini-X's spectral output; however, there is an energy resolution trade-off that is imposed when the peaking time is adjusted. When detecting radiation, it is more favorable for a given energy peak to have a narrow pulse height distribution, so that any deviations from the expected energy value are minimal [28]. However, as seen in Figure 4.8, the detector energy resolution decreases as the peaking time is shortened, which in effect, broadens the pulse height distribution. Figure 4.9 further demonstrates this.

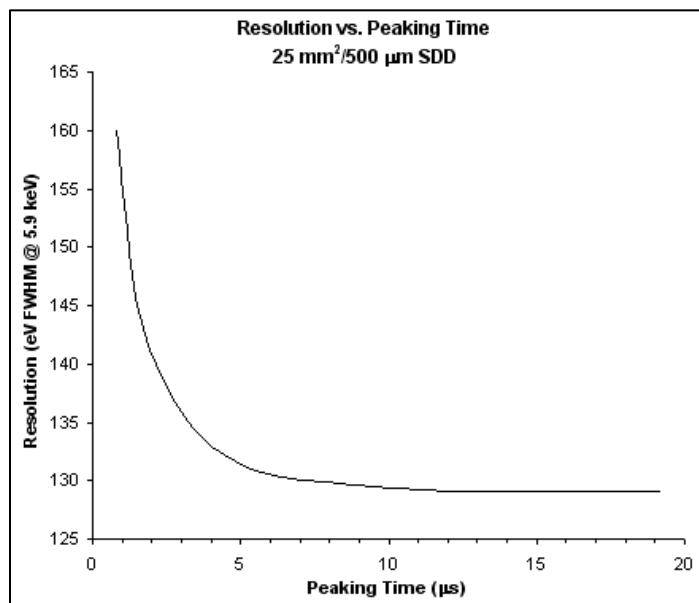


Figure 4.8 Energy resolution versus peaking time [29]

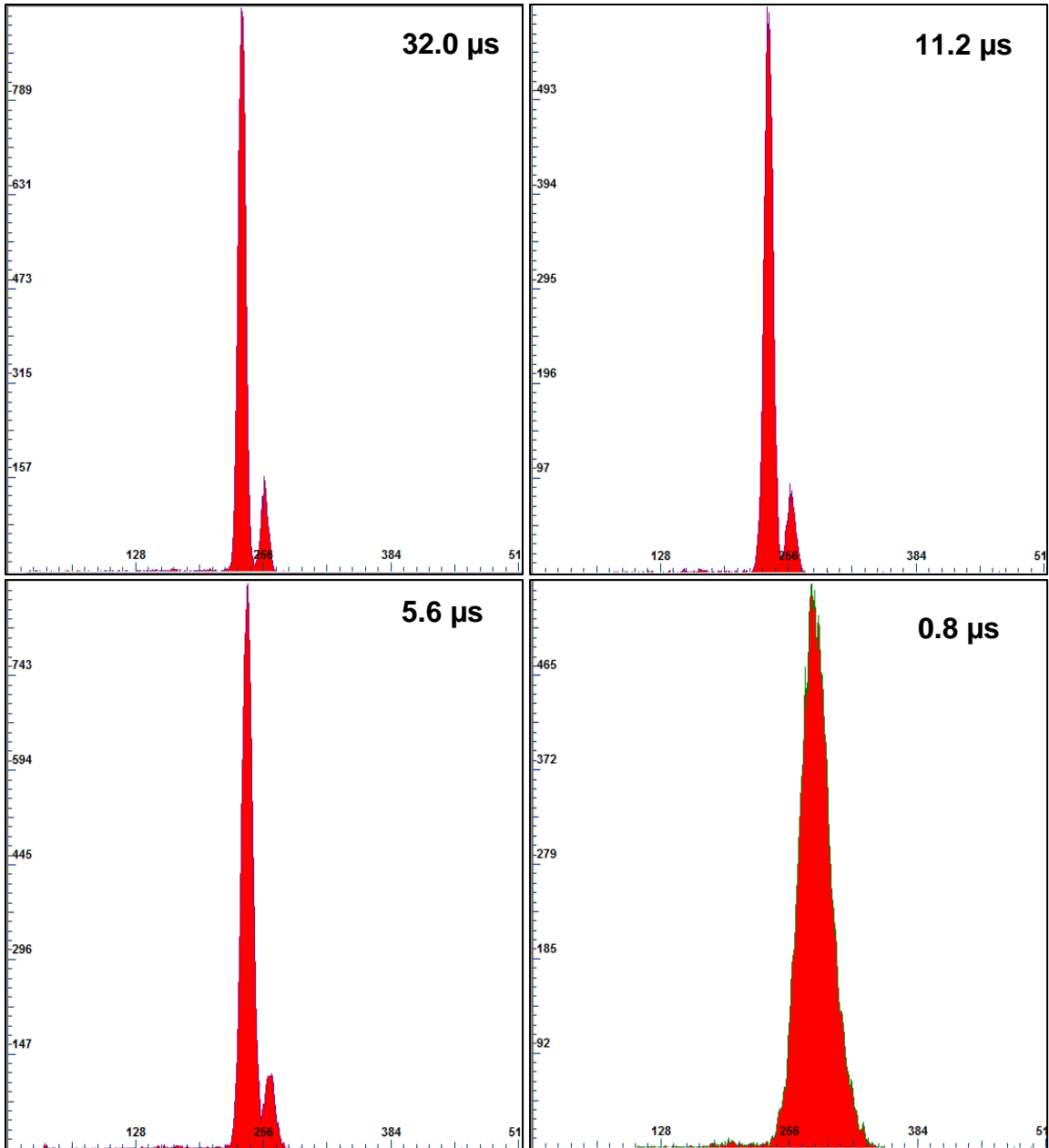


Figure 4.9 Experimental analyses of peaking time and energy resolution

The spectra in Figure 4.9 were obtained using an iron-55 source. These spectra illustrate the effect that the peaking time has on x-ray detection. As expected, the energy resolution clearly broadens as the peaking time is changed. What is also seen is that the energy peaks begin to overlap as the peaking time is decreased. Given Figure 4.8 and the results illustrated in Figure 4.9, it was decided that a peaking

time of 4.8 μs or more was to be used for all measurements. This would reduce the effects of high count rates at the detector, without having to sacrifice significantly on energy resolution. At this peaking time, the detector has an allowable count rate of about 30000 cps before dead time effects become apparent. In order to get the Mini-X count rate down to a level where dead time effects were minimal, a brass collimator was fixed to the detector.

4.4 X-Ray Spectroscopy

It is important to know what the actual Mini-X output spectrum is in order to properly interpret the experimental results. Therefore, analysis was done to determine the Mini-X's output spectrum for filtered and unfiltered arrangements. Table 4.5 below shows all the filters that were supplied with the Mini-X. However, only the 254 μm aluminium filter was used for this analysis.

Material	Thickness (μm)
Aluminium (Al)	1016
Aluminium (Al)	254
Copper (Cu)	25.4
Molybdenum (Mo)	25.4
Silver (Ag)	25.4
Tungsten (W)	25.4

Table 4.5 List of Mini-X filters

The operating voltage and current were set to 20 kV_p and 5 μA respectively. For all spectra, the maximum photon energy is 20 keV, and any counts registered for any energy above this are due to detector pulse pile-up. Also, the detector was calibrated from channel number to energy with the use of an iron-55 source⁸.

⁸ See Figure 4.9 for examples of iron-55 spectra

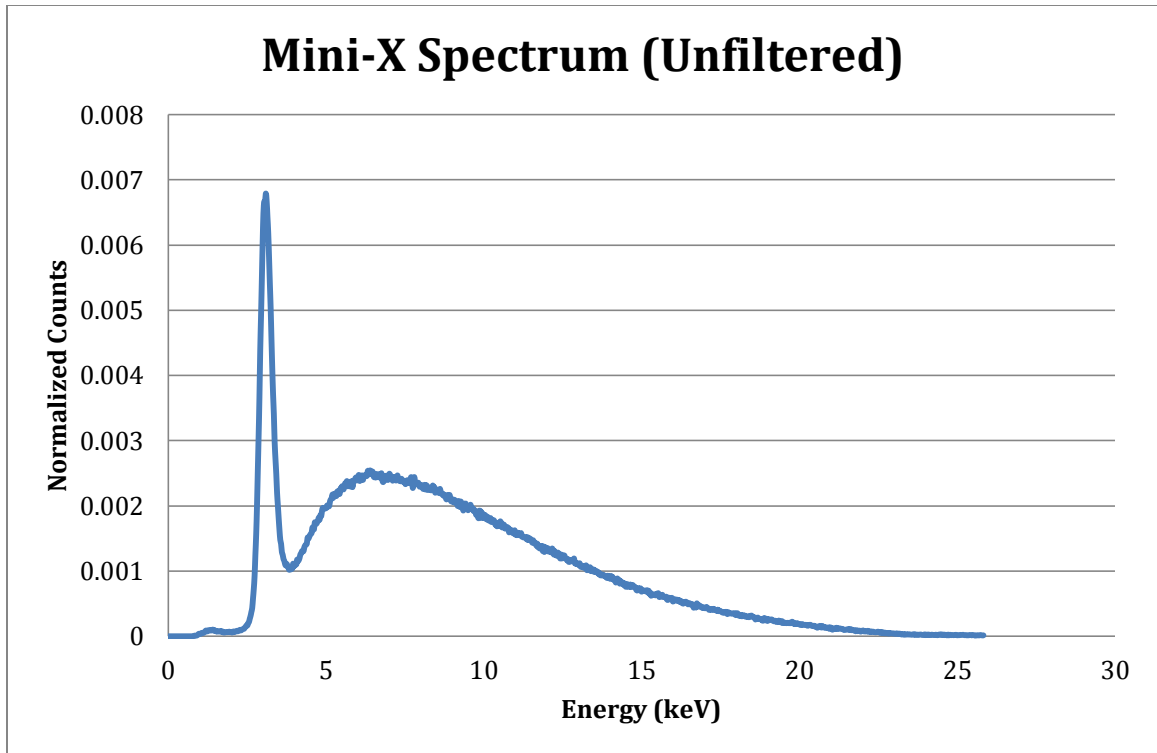


Figure 4.10 Unfiltered Mini-X spectrum at 20 kV_p

Figure 4.10 shows the unfiltered Mini-X spectrum. Along with the expected bremsstrahlung continuum, there is also a sharply defined peak at about 3.04 keV. Recalling that the Mini-X uses silver to generate x-rays, it becomes apparent that this peak is silver's L_{α} and L_{β} characteristic x-rays, which have energies of 2.98 keV and 3.15 keV respectively. The presence of this peak makes the unfiltered spectrum more appealing, because one can take advantage of these low energy x-rays to mimic the tritium decay spectrum.

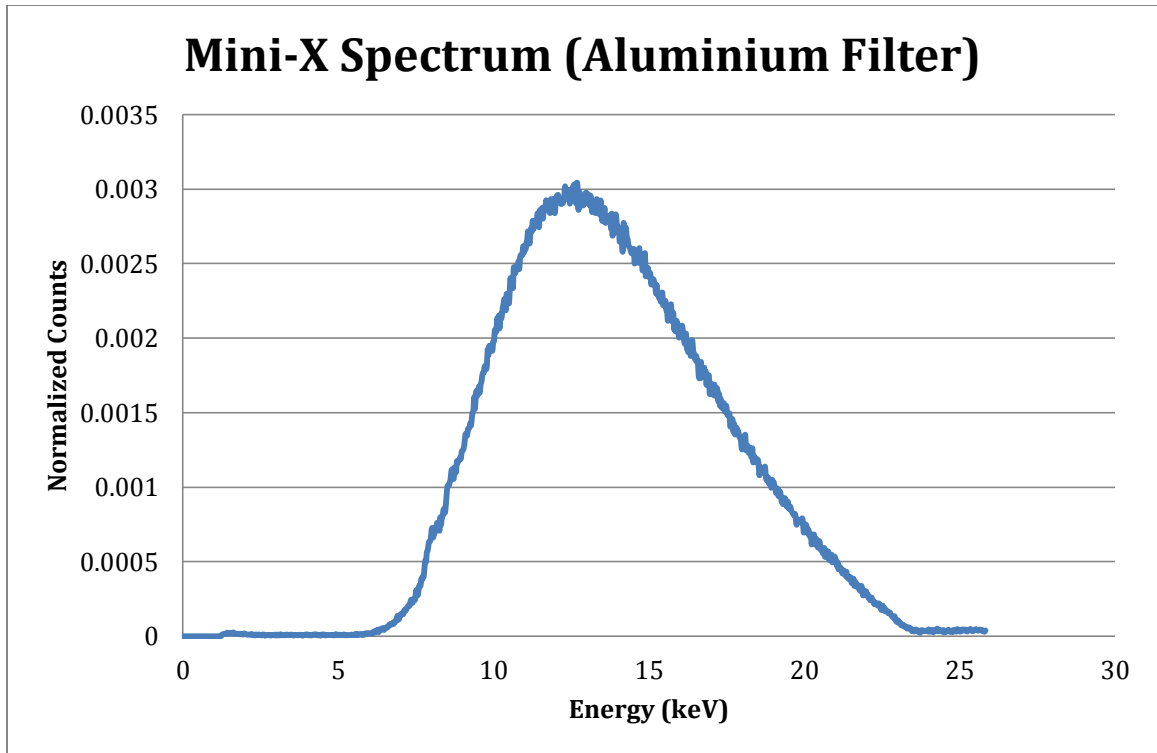


Figure 4.11 Filtered Mini-X spectrum at 20 kV_p

Figure 4.11 shows the aluminium filtered output spectrum. As expected, many of the lower energy photons have been filtered out, particularly those below about 6 keV. This spectrum is slightly different from the 20 kV_p spectrum shown in Figure 3.3, but the differences could be attributed to different filters being used. A marked decrease of the detected count rate from the unfiltered beam (~57932 cps) to the filtered beam (~40469 cps) was also noted.

4.5 Characteristic X-Ray Experimental Results

Experimental work was carried out mainly to compare and contrast the results obtained from the Mini-X simulations with iron and titanium. An aluminium filter was used to reduce the count rate such that it was low enough for dead time effects to be minimal, with the detector placed roughly 2 mm from the target. As noted in chapter 3, an iron-55 source was used to calibrate the channel axis of the MCA. The spectra obtained for iron and titanium are shown in Figures 4.12a and 4.12b (page 64). A comparison between the experimental and simulation results are also shown in Figures 4.13a and 4.13b (page 65). Figures 4.12a and 4.12b essentially confirm the results from the simulation, and further demonstrate that characteristic x-rays may not be a useful method for mimicking a tritium spectrum. The photon energy peaks for both materials are visible, but the vast majority of the photons collected were from the Mini-X source. Also see in both spectra are two small peaks at about 8 and 8.5 keV. These peaks are the characteristic x-rays of copper and zinc, which are the main constituents of the detectors brass collimator. Comparing experimental with the simulated, it is seen that the characteristic x-ray peaks are in good agreement. However, where the spectra differ the most is the energy distribution for the detected source photons. The main reason for these discrepancies is largely due to the fact that the simulated x-ray source (Figure 4.4) was slightly different from the filtered x-ray spectra (Figure 4.11). Even so, the obtained experimental and simulated spectra both exhibit similar trends for the detected source photons.

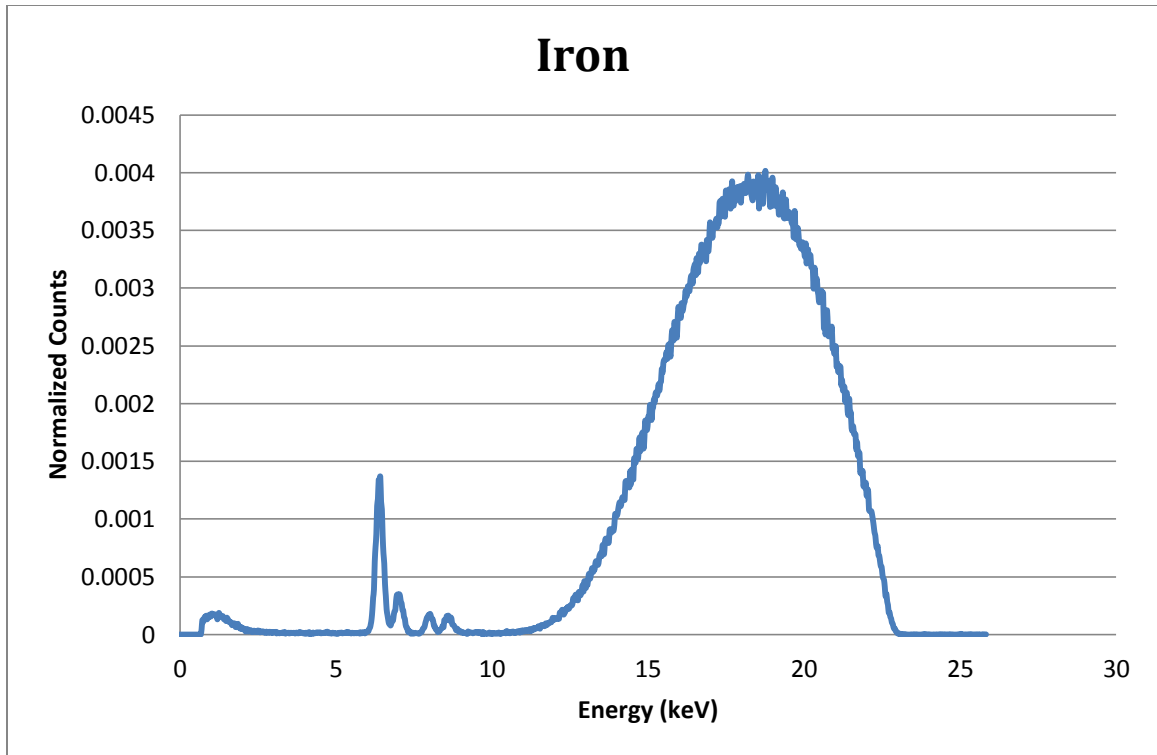


Figure 4.12a Experimental x-ray spectra for iron

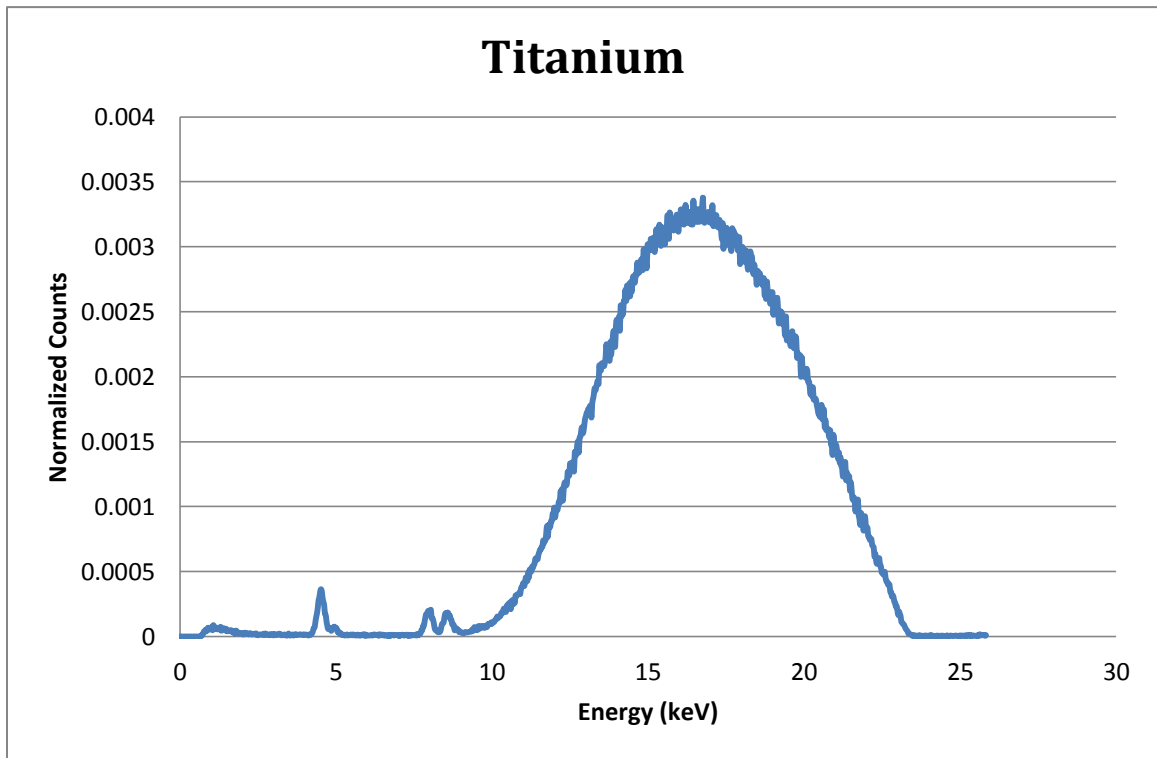


Figure 4.12b Experimental x-ray spectra for titanium target

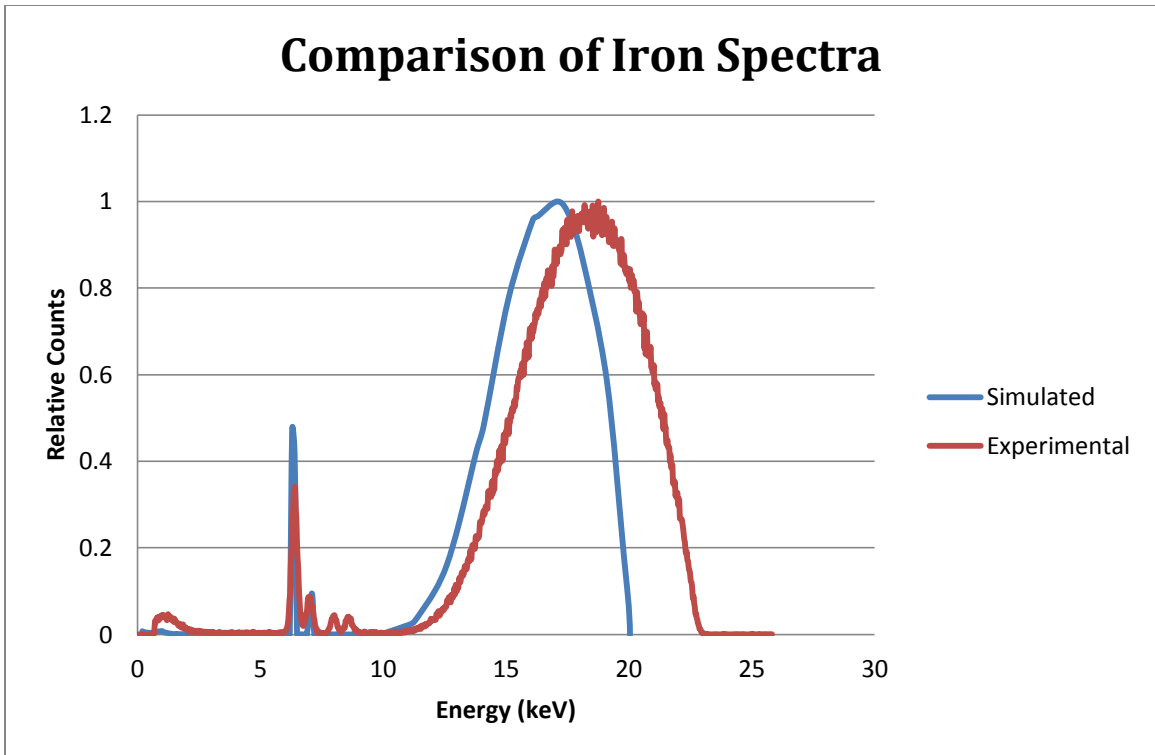


Figure 4.13a Comparison of experimental and simulation spectra for iron

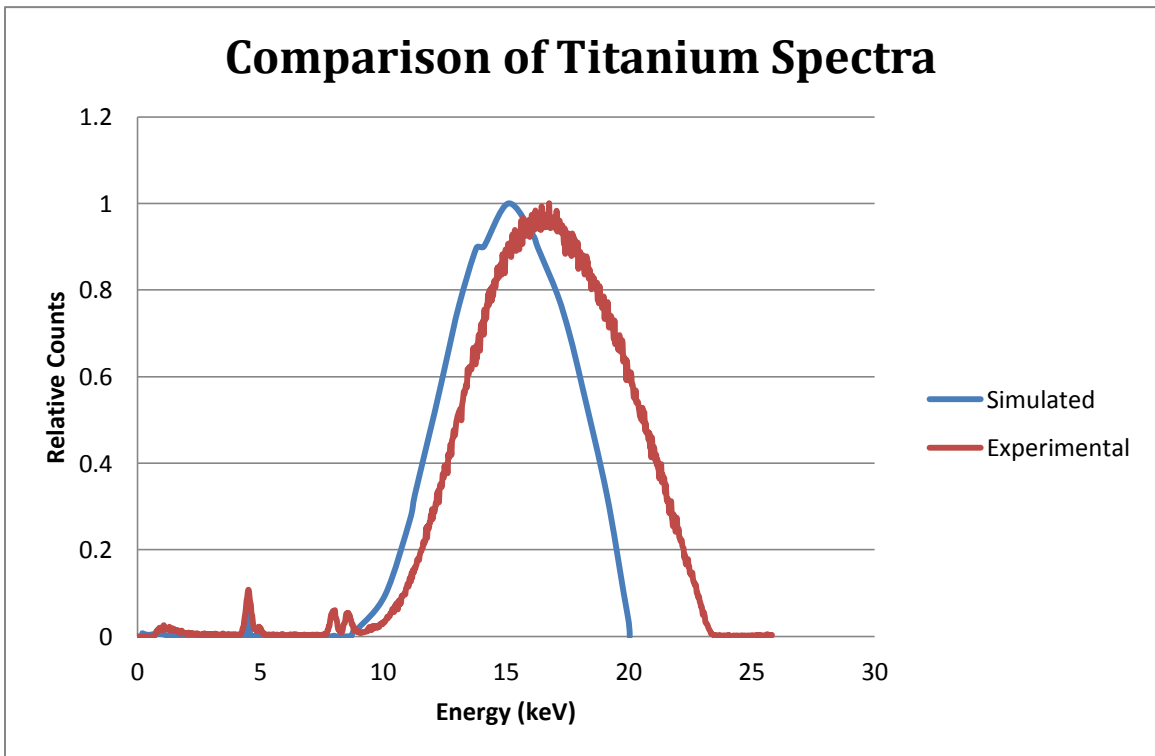


Figure 4.13a Comparison of experimental and simulation spectra for titanium

4.6 Electron Spectrum in Water

In order to determine the resultant electron energy distribution in water, simulations were carried out. Since the characteristic x-ray results were unfavorable, attention was turned to investigating the primary electron spectrum generated in water, by a simulated unfiltered Mini-X source. Figure 4.14 shows a spectral comparison between the tritium beta decay energy spectrum and the unfiltered Mini-X source.

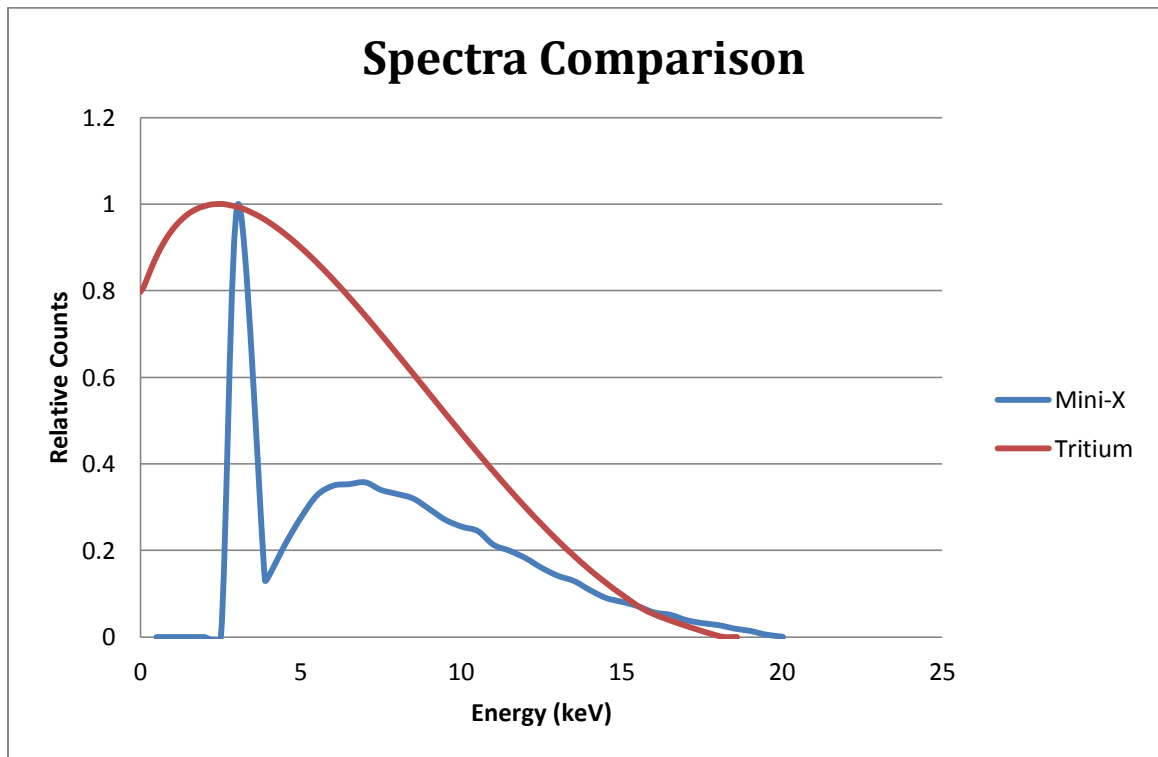


Figure 4.14 Spectra comparison of Mini-X and tritium

As seen in Figure 4.14, in order for the Mini-X spectrum to mimic tritium, some of the L x-rays would have to be absorbed. This could be accomplished with a thin filter that absorbs low energy x-rays well. It was decided that aluminium would be a suitable absorber material.

The optimal thickness, t , of the aluminium filter can be determined by rearranging Equation 2.1b:

$$t = -\frac{\ln(P)}{\mu_m \rho} \quad 4.5$$

Aluminium has a density of 2.7 g/cm³ [31], and at 3 keV (energy of silver L x-ray), the total mass attenuation coefficient is 788.1 cm²/g [18]. For a 50% transmittance of the 3 keV x-rays, the thickness is calculated as:

$$t = -\frac{\ln(0.5)}{(788.1)(2.7)} = 3.27 \mu\text{m}$$

Materials were purchased from a company called Goodfellow, and according to their catalogue, the closest thickness to the above calculation is 3 μm [34]. A simulation was done with an aluminium filter of this thickness to confirm that it would absorb enough photons to improve the spectrum.

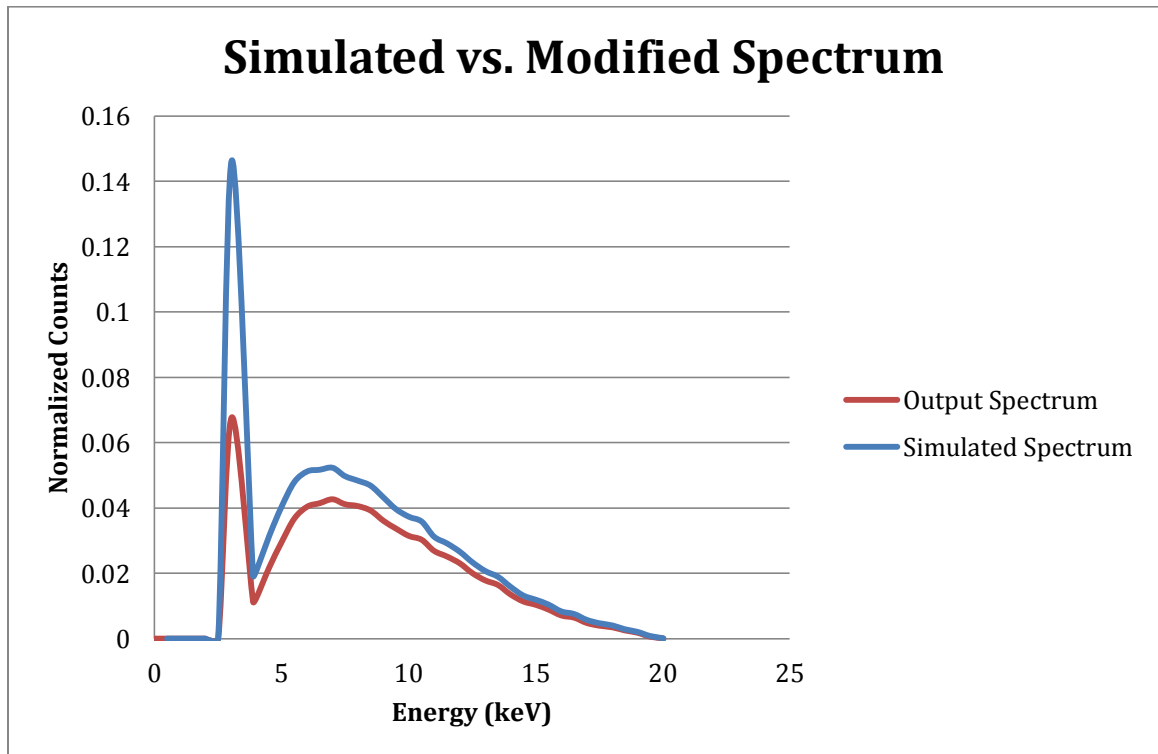


Figure 4.15 Comparison of simulated x-ray spectrum with filtered spectrum

As seen in the Figure 4.15, the aluminium filter successfully absorbed many of the 3 keV x-rays, without drastically affecting the higher energy x-rays. Given this result, simulations were performed to determine the resultant primary electron spectrum in water, for slab thicknesses of 2 mm and 3 mm.

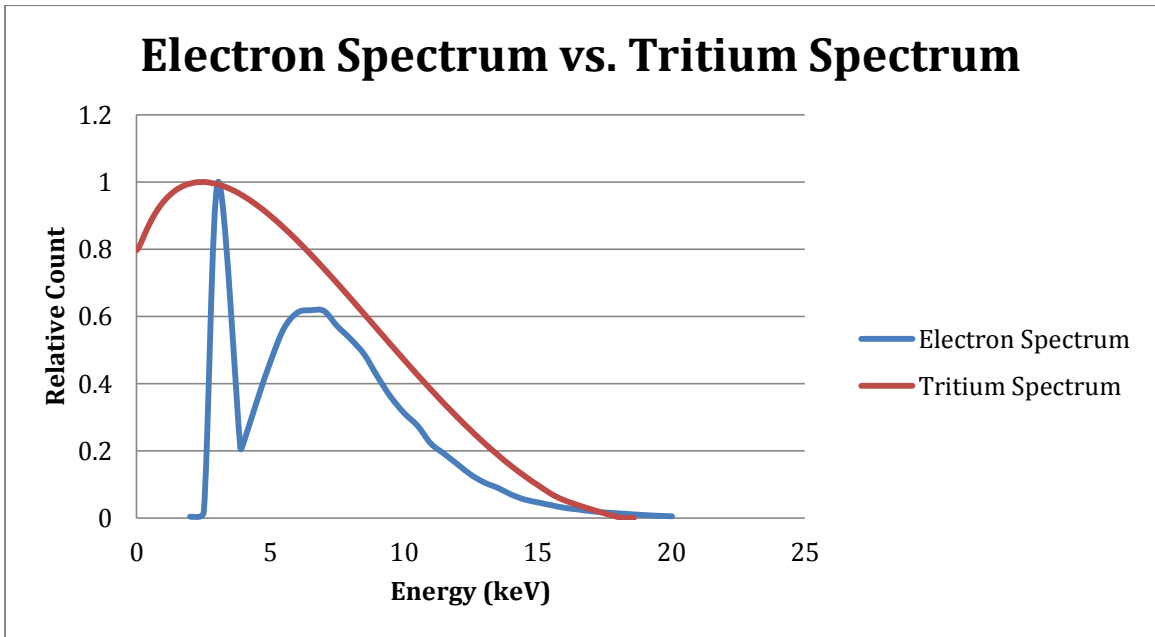


Figure 4.16a Electron spectrum for 2 mm water slab

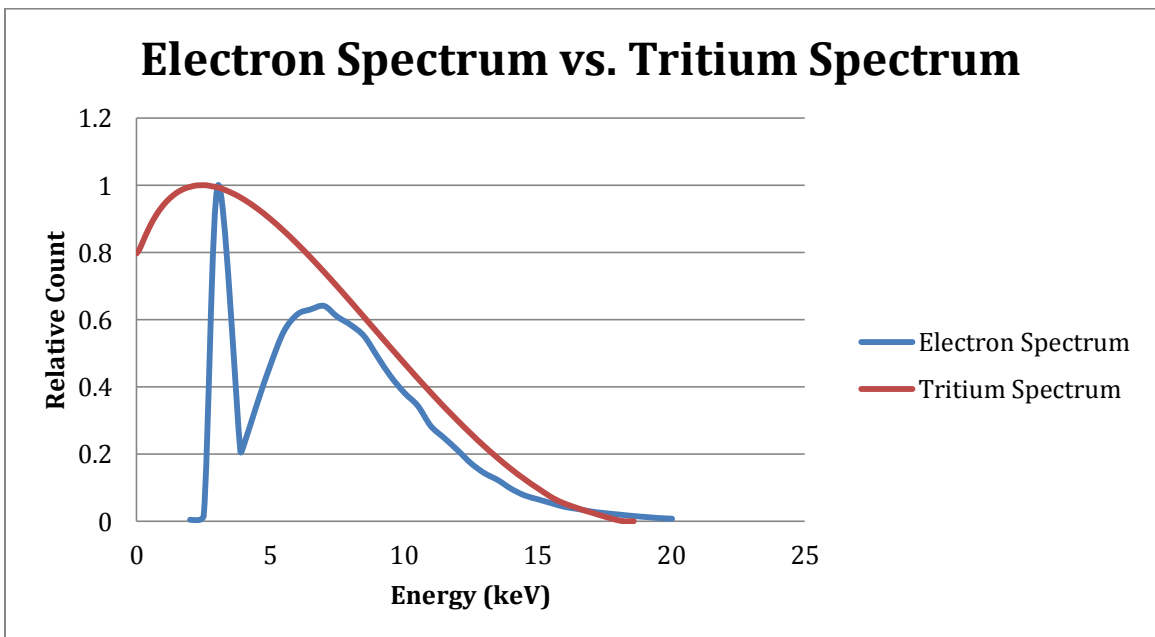


Figure 4.16b Electron Spectrum for 3 mm water slab

The results from the simulations are shown in Figure 4.16a and 4.16b. The electron spectrum that was generated is strikingly similar to the modified Mini-X spectrum; this indicates that the photoelectric effect is the dominant interaction mode of the photons. It must be noted, however, that a portion of the higher energy photons were lost due to transmittance through the water slab. This is evident when comparing the tail-end of the electron spectrum for both figures. It is reasonable to conclude that for a “large” water slab, the vast majority of the source photons will interact photoelectrically, thus resulting in an electron spectrum matching the source spectrum. The more important aspect though, is for the electron spectrum to match the tritium spectrum; an appropriate water slab thickness would have to be chosen to accomplish this.

The most notable result from these simulations however, is that the electron spectrum does not match the tritium spectrum, which was to be expected. As seen, the electron spectrum is missing a large portion of the low energy spectrum. This is obviously an issue since the lower energy electrons will have higher LETs. For example, in water, 1 keV and 10 keV electrons have LET values of 12.6 keV/ μm and 2.32 keV/ μm , respectively [2]. However, it should be emphasized that Figures 4.16a and 4.16b show the primary electron spectrum (ie. electrons generated from interactions with the source photons). These primary electrons will deposit their energy in the water slab, transferring their energy to other molecular electrons, which results into an electron spectrum that will be distinct from the ones shown. To determine how this spectrum would look would require a Monte Carlo transport

code that models every electron interaction; unfortunately, MCNP is not suitable for this task. Even so, the simulation results do indicate that the use of photons is a promising method for simulating a tritium exposure in tissue or water.

CHAPTER 5 CONCLUSION

The purpose for the research described in this thesis was largely directed at uncertainties regarding the dosimetry of low energy electrons (beta particles). Focus was centered on tritium in particular because it is a low energy beta emitter, and is a radionuclide to which CANDU workers can be exposed. Due to some limitations of using tritium for biophysics experiments, the main objective of this thesis was to investigate the use of photons to simulate a tritium exposure in water (and consequently tissue). The use of photons to simulate tritium is theoretically practical, because at the energies considered for this thesis, the photoelectric effect is the dominant mode of interaction. Therefore, when a photon interacts with a molecular electron in water, it will transfer all of its energy to that electron.

This thesis first focused on specifications regarding the x-ray source, and possibly modifying the output spectrum of the source with characteristic x-rays. The target materials chosen for characteristic x-ray analysis were titanium and iron because their K x-ray energies were in the region of interest (~ 4 to 6 keV). However, the results indicate that characteristic x-rays are not a viable means for modifying the Mini-X spectrum, because not enough characteristic x-rays escape the target in the forward direction. Given these results, focus was placed on analyzing the characteristics of the Mini-X's output spectrum.

Analysis of the Mini-X output spectrum at 20 keV showed that for an unfiltered beam, the silver target's L x-rays made a significant contribution to the overall spectrum. This contribution, however, was much more intense than the bremsstrahlung continuum, thus, the use of an aluminium absorber was therefore needed to filter out some of the L x-rays. Using this aluminium filtered spectrum, simulation results showed that the primary electron spectrum in water was noticeably different from the x-ray spectrum at the tail end. As noted however, it is of more importance that the electron spectrum matches the tritium spectrum, and the tail end of the electron spectrum is doing so as the slab thickness is increased. Although the results seem promising, the major limitation seems to be that the primary electron spectrum is missing electron energies below 3 keV, and the spectrum is less intense around the 4 to 6 keV region than required. It should be stressed however, that the slowing down electron spectrum will be different from the primary electron spectrum. This difference between the spectra may be significant, but it is unclear at this point if this spectrum will be closer to matching tritium or not.

Future work should further investigate the electron spectrum generated in water with a Monte Carlo code that simulates the transport of electrons more accurately. Suitable codes would be PENELOPE or the Oak Ridge Electron transport Code (OREC). If the slowing down electron spectrum is no closer to mimicking tritium, then other methods may have to be taken into consideration. There are certain constraints associated with x-ray generation however, especially with

regards to what targets can be used to generate a beam. As such, due to the design constraints of x-ray generators it will be difficult to generate x-rays with energies below 3 keV. The beam obtained with the aluminium absorber may be the best that can be done with the current setup, and if so, further work should also look into using this setup for biophysics experiments.

It is strongly recommended that the Mini-X be characterised using a calibrated ionization chamber and a 2D dosimeter, such as radiochromic film, in order to map the beam spread and dose rate uniformly. Microdosimetric measurements should also be carried out using a wall-less proportional counter to determine the degree of similarity between tritium beta particles and the x-ray beam in terms of microdosimetric quantities. Doing so would also reflect the effect of the slowing down electron spectrum.

**APPENDIX A
RAW DATA TABLES**

TRITIUM BETA DECAY DATA [11]							
Energy (keV)	Count	Normal Count	Relative Count	Energy (keV)	Count	Normal Count	Relative Count
0	82.18	0.015997	0.79709	1.4	100.2	0.019505	0.971872
0.1	83.33	0.016221	0.808244	1.5	100.8	0.019622	0.977692
0.11	83.5	0.016254	0.809893	1.6	101.3	0.019719	0.982541
0.12	83.67	0.016287	0.811542	1.8	102.1	0.019875	0.990301
0.13	83.85	0.016322	0.813288	2	102.6	0.019972	0.99515
0.14	84.03	0.016357	0.815034	2.2	103	0.02005	0.99903
0.15	84.21	0.016392	0.81678	2.4	103.1	0.020069	1
0.16	84.4	0.016429	0.818623	2.6	103.1	0.020069	1
0.18	84.78	0.016503	0.822308	2.8	102.8	0.020011	0.99709
0.2	85.16	0.016577	0.825994	3	102.5	0.019953	0.99418
0.22	85.55	0.016653	0.829777	3.2	102	0.019855	0.989331
0.24	85.93	0.016727	0.833463	3.6	100.6	0.019583	0.975752
0.26	86.31	0.016801	0.837148	4	98.8	0.019232	0.958293
0.28	86.69	0.016875	0.840834	4.5	96.03	0.018693	0.931426
0.3	87.07	0.016949	0.84452	5	92.78	0.01806	0.899903
0.32	87.45	0.017023	0.848206	5.5	89.15	0.017354	0.864694
0.36	88.18	0.017165	0.855286	6	85.21	0.016587	0.826479
0.4	88.89	0.017303	0.862173	6.5	81.01	0.015769	0.785742
0.45	89.76	0.017473	0.870611	7	76.62	0.014915	0.743162
0.5	90.58	0.017632	0.878565	7.5	72.08	0.014031	0.699127
0.55	91.38	0.017788	0.886324	8	67.44	0.013128	0.654122
0.6	92.14	0.017936	0.893695	8.5	62.74	0.012213	0.608535
0.65	92.85	0.018074	0.900582	9	58.01	0.011292	0.562658
0.7	93.54	0.018208	0.907275	10	48.62	0.009464	0.471581
0.75	94.19	0.018335	0.913579	11	39.52	0.007693	0.383317
0.8	94.82	0.018458	0.91969	12	30.94	0.006023	0.300097
0.85	95.41	0.018572	0.925412	13	23.06	0.004489	0.223666
0.9	95.97	0.018681	0.930844	14	16.07	0.003128	0.155868
1	97.01	0.018884	0.940931	15	10.15	0.001976	0.098448
1.1	97.95	0.019067	0.950048	16	5.452	0.001061	0.052881
1.2	98.78	0.019228	0.958099	18	0.3067	5.97E-05	0.002975
1.3	99.53	0.019374	0.965373	18.6	0	0	0

Energy (keV)	Mass Attenuation Coefficient (cm ² /g)	
	Compton	P.E.
1	0.01319	4076
1.5	0.02673	1374
2	0.04184	616.2
3	0.07075	191.9
4	0.0943	81.97
5	0.1123	41.92
6	0.1259	24.07
8	0.144	9.919
10	0.155	4.944
15	0.1699	1.369
20	0.1774	0.5439

APPENDIX B DOCUMENTATION FOR REGISTRATION OF MINI-X

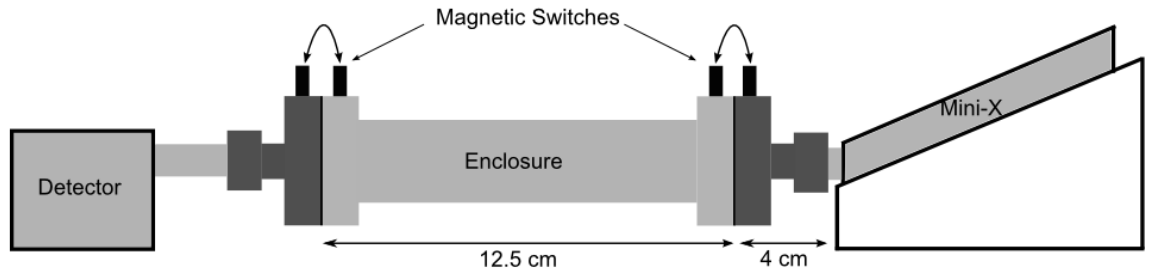


Figure B1. Mini-X Mounting Rig and Enclosure

Figure B1 is a diagram of the planned experimental setup for the Mini-X. The Mini-X itself is mounted to the laboratory work bench. When connected to the Enclosure, the Mini-X x-ray beam is totally contained, and no radiation should be detectable outside of the enclosure. Additionally, an interlocking mechanism has been setup such that the Mini-X can only be operated when the enclosure is connected.

Mini-X and Detector



Figure B2. Detector (left) and Mini-X (right)

Figure B2 shows both the detector and Mini-X. The Mini-X is a miniature x-ray tube that uses a silver target to generate x-rays. The Mini-X has a maximum operating voltage of 40kV, and the output beam is collimated to a 5° cone. The detector is a silicon drift detector. Both the Mini-X and the detector use conflat (seen in Figure B2) to connect to the enclosure. Both the Mini-X and detector are software controlled on a password protected PC, which is only accessible to users trained to use the Mini-X. The location of the PC with respect to the Mini-X is shown in Figure B3, and the user will be present at all times while the Mini-X is in use.

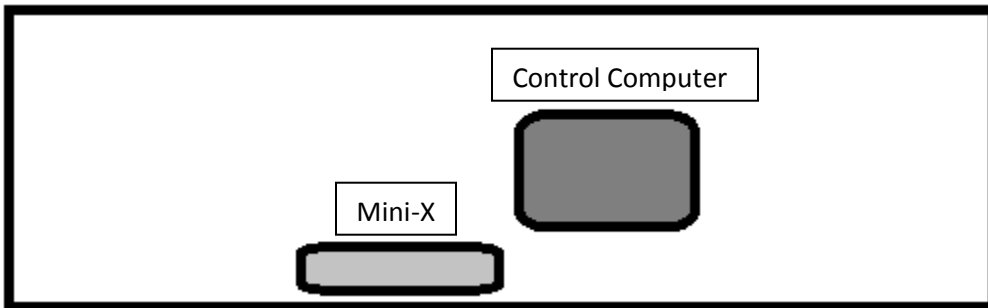


Figure B3. Mini-X and Control Computer

Enclosure



Figure B4. Enclosure

Figure B4 shows the enclosure that will be used. The detector and Mini-X will be attached to the larger ends of the enclosure. Blank conflat will be used to close off

the shorter ends. As shown in Figure B1, the enclosure is 12.5 cm long, and has a wall thickness of about 4.04 mm. Given that the enclosure is made up of 304L stainless steel, a thickness of 4.04 mm is more than enough to shield 40 keV photons (maximum Mini-X x-ray energy).

The following table shows the material and composition of 304L steel, as well as the mass attenuation coefficient for each element at 40keV.

Element	Composition	Mass Attenuation (cm²/g)
Carbon	0.03	0.2076
Manganese	2.00	3.1690
Phosphorus	0.045	0.8096
Sulfur	0.030	0.9872
Silicon	0.750	0.7012
Chromium	18.00	2.8560
Nickel	8.00	4.6000
Aluminium	0.10	0.2288
Iron	70.995	3.6290

Table B1 Physical data for 304L stainless steel [24] [18]

The linear attenuation equation is given as:

$$I = I_0 e^{-\mu x} \quad \text{B1}$$

From this equation, the probability that a photon will traverse a distance x through a given material is:

$$P = \frac{I}{I_0} = e^{-\mu x} \quad \text{B2}$$

By using this equation we can determine how well the stainless steel wall can shield 40 keV photons. Since stainless steel is a composition of various materials, its mass attenuation coefficient is determined by:

$$\left(\frac{\mu}{\rho}\right)_{comp} = \frac{\sum_i \left(\frac{\mu}{\rho}\right)_i C_i}{\sum_i C_i} \quad \text{B3}$$

Where $\left(\frac{\mu}{\rho}\right)_i$ and C_i are the mass attenuation and composition for a given element.

Given that the density of 304L stainless steel is 8.03 g.cm^{-3} , the composite linear attenuation is found to be:

$$\mu_{comp} = \rho * \left(\frac{\mu}{\rho}\right)_{comp} = (8.03) * (3.5299) = 28.345 \text{ cm}^{-1}$$

Using this information in Equation B2, we can determine how well the enclosure shields the photons:

$$P = e^{-\mu x} = e^{-(28.345)(0.404)} = 0.000010635 (\sim 0.001\%)$$

Therefore, a 40 keV photon roughly has a **0.001%** chance of escaping our enclosure, and thus serves as adequate shielding. It can be further noted that 40 keV will be the maximum energy of x-rays produced and that the majority of x-rays generated by the Mini-X operated at 40 kV will be much less. The mean energy of x-rays produced in the Mini-X at 40 kV is around 22-25 keV which will have a much smaller probability of escape.

Interlocking and Safety System



Figure B5. Mini-X interlocking mechanism

Figure B5 is the back end of the Mini-X. Pins 1 and 2 are used to enable the Mini-X; a circuit has been implemented with our Mini-X to control its interlocking system, and will be discussed below. Pins 3 and 4 are used for optional external safety mechanisms. When the Mini-X is in use, there is an LED that flashes on the back of the unit (the LED is labeled “J3” on the image to the right). Warning ‘beeps’ are also given off when the Mini-X is in use.

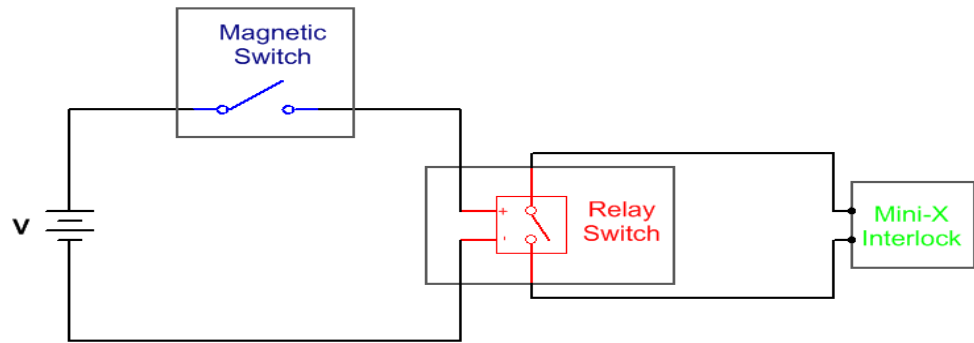


Figure B6. Schematic of Safety Circuit

Figure B6 shows a schematic of the circuit used to control the Mini-X interlock. Referring to Figure B5, pins 1 and 2 must be connected in order for the Mini-X to produce x-rays. A safety circuit has been developed that allows the enclosure and the conflat to act as contact switches. In other words, the Mini-X will only operate when the enclosure and conflat are attached.

The **Magnetic Switches** are fixed to the conflat and enclosure; the locations of these are shown in Figure B1. The **Relay Switch** is connected to the **Mini-X Interlock**, and is normally opened; the **Relay Switch** will close only when the **Magnetic Switch** is also closed (ie. conflat and enclosure are attached), thus

enabling the Mini-X for use. If the enclosure is removed while the Mini-X is producing x-rays, both the **Magnetic Switch** and the **Relay Switch** will open, which will disable Mini-X from producing x-rays. If the enclosure is reconnected, the user will have to restart the Mini-X manually.

Mounting Rig for Mini-X

The Mini-X mounting rig is made out of wood and has been permanently fixed to the lab bench in room ERC 3054. The dimensions and setup of the rig can be seen in the figures below.

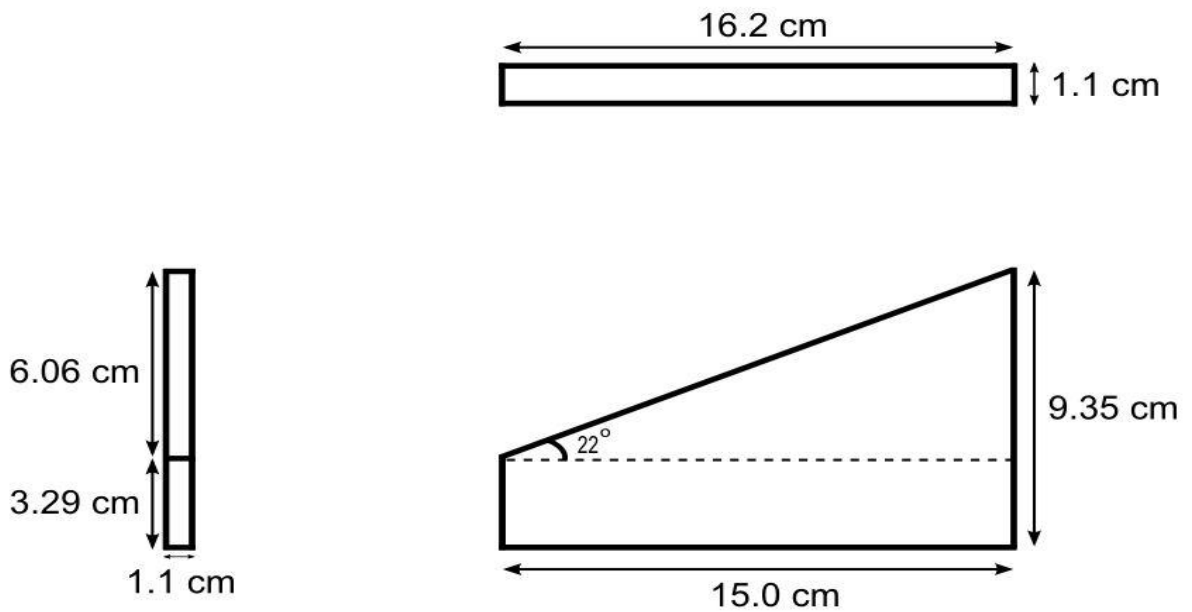


Figure B7. Mounting Rig

Ministry of Labour

Radiation Protection Services

Occupational Health and Safety Branch
81A Resources Road
Toronto, Ontario
M9P 3T1

Telephone: 416 235-5922
Fax: 416 235-5926

Ministère du Travail

Services de radioprotection

Direction de la santé et de la sécurité au travail
81A Resources Road
Toronto (Ontario)
M9P 3T1

Téléphone : 416 235-5922
Télécopieur : 416 235-5926



July 12, 2012

Mr. David Gorman, Radiation Safety Officer
University of Ontario Institute of Technology
2000 Simcoe Street North
Oshawa, ON L1H 7K4

RPS Registration No.: O-11666

RE: X-ray Source Installation – Amptek Mini-X Tube and Enclosure

Dear Mr. Gorman:

Your application, for review of a permanent X-ray location, is accepted in compliance with section 6 of O.Reg. 861/90 – the Regulation Respecting X-ray Safety. University of Ontario Institute of Technology is registered as an employer in possession of the referenced X-ray source applied for at the above address under registration number: **O-11666**.

The radiation shielding and safety provisions (designation of a competent person, location of the X-ray source, and controls, X-ray room layout, and the type and location of safety devices such as warnings signs, warning lights, interlocks and cut-off switches) as indicated on the Forms and plan location drawing(s) appear to be acceptable. Enclosed for your records is a copy of the plan location drawing, bearing the Ministry of Labour's stamp.

Please note that any change to the installation or use of the X-ray source, or use of adjacent rooms or areas, or a change in the shielding that may result in an increase in the exposure of a worker, the X-ray source shall not be used unless the change has been reviewed by and is acceptable to an inspector. In addition, the employer must give immediate notice to the Director if the employer ceases to have possession of the X-ray source (i.e. sale, transfer or disposition of the X-ray source).

If you have any questions or concerns regarding this letter, please do not hesitate to contact this office at 416-235-5922.

Sincerely,

A handwritten signature in black ink, appearing to read "E. Fregonese".

Edward S. Fregonese
Radiation Protection Officer
Ontario Ministry of Labour

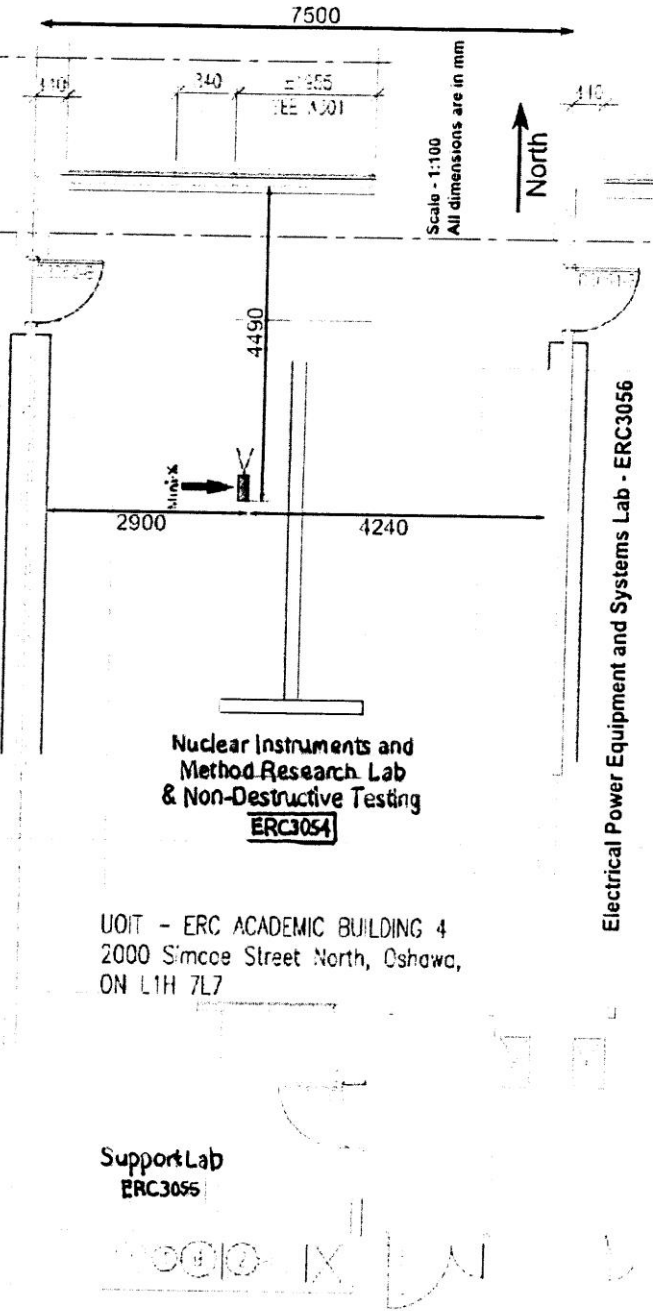
Encl. MOL Stamped Plan Drawing

 ONTARIO MINISTRY OF LABOUR Radiation Protection Services	Plan accepted as in Compliance with Ontario Regulation 861/90 X-ray Source Location Reviewed by:
	<i>Edward Frisfort</i> Edward Frisfort 2607 Ave
Regulation Number: <u>0-11666</u>	

RADIATION PROTECTION SERVICE
 Occupational Health and Safety Branch
 51A Redoubt Road
 WESTON, ONTARIO
 MSP 3T1

15430

Scientific Instrumentation & Control Lab - ERC3052



APPENDIX C

MCNP CODES WRITTEN FOR THESIS

Characteristic X-Ray Simulations

This MCNP code corresponds to an input file for a titanium characteristic x-ray simulation with a simulated Mini-X source, however, values that are seen in parentheses can be adjusted to suit a different problem for simulation. For example, to simulate an iron target, the target density must be changed to -7.86, the target thickness to 0.007502 and the first entry for the material card must be changed to 26000.

X-ray Source

```

c
c Simulation of characteristic x-rays
c *****Cell Block*****
c -----
1 1  -4.510 -1 2 -3          $Target
2 2  -2.329 -11 12 -13       $Detector
3 0      #(-1 2 -3)         $Universe
      #(-11 12 -13)
      -21
4 0      21                  $Void

c *****Surface Block*****
c -----Target-----
1 cz  0.1                    $Target Radius
2 pz  0.00002
3 pz  0.01002                $Target Thickness
4 cz  0.01

c -----Detector-----
11 cz  0.5                   $Detector Radius
12 pz  0.10752               $Surface 12 and 13 form the
13 pz  0.157520             $cell for the detector
c -----Universe-----
21 so  4

c *****Data Block*****
c -----Cell Importances-----
mode p e
imp:p  1 1 1 0
imp:e  1 1 0 0
c -----Material Card-----
M1 22000  1.0
M2 14000  1.0              $detector material
c -----Source Definition-----

```

```
sdef pos=0 0 0 axs=0 0 1 rad=d1 erg=d2 par=2 vec=0 0 1 dir=1
c
si1 0 (0.04)
sp1 -21 1
c
si2 L 0.00200 0.00250 0.00300 0.00375 0.00400 0.00500 0.00600 0.00625 0.00700
0.00750 0.00800 0.00875 0.00900 0.01000 0.01100 0.01125 0.01200 0.01250
0.01300 0.01375 0.01400 0.01500 0.01600 0.01625 0.01700 0.01750 0.01800
0.01900 0.01975 0.02000
c
sp2 0.00246 0.00246 0.00246 0.00328 0.00328 0.01392 0.03522 0.04361 0.05651
0.06224 0.06634 0.06818 0.06798 0.06634 0.06061 0.05876 0.05405 0.05078
0.04750 0.04197 0.03931 0.03440 0.02703 0.02580 0.02129 0.01802 0.01474
0.00819 0.00246 0.00082
c
f8:p 2
E8:p 0 199i 0.02
nps 10000000
```

Electron Spectrum in Water Simulations

X-ray Source

c *****Cell Card*****

c -----

```
1 1 -2.700 -1 2 -3      $Target filter
2 2 -1.000 -11 12 -13   $Detector
3 0      #(-1 2 -3)     $Universe
                #(-11 12 -13)
                -21
4 0      21             $Void
```

c *****Surface Card*****

c -----Target-----

```
1 cz  0.1              $Target Radius
2 pz  0.00002
3 pz  0.00032          $Target Thickness
4 cz  0.01
```

c -----Detector-----

```
11 cz  0.2             $Detector Radius
12 pz  0.000330        $Surface 12 and 13 form the
13 pz  0.200330        $cell for the detector
```

c -----Universe-----

```
21 so  4
```

c *****Data Card*****

```
mode p e
```

```
imp:p 1 1 1 0
```

```
imp:e 1 1 0 0
```

c -----Material Card-----

```
M1 13000  1.0
```

```
M2  1000  2.0  8000  1.0
```

c -----Source Definition-----

```
sdef pos=0 0 0 axs=0 0 1 rad=d1 erg=d2 par=2 vec=0 0 1 dir=1
```

c

```
si1 0 0.04
```

```
sp1 -21 1
```

c

```
si2 L 0.000501 0.001009 0.001518 0.002001 0.002510 0.003044 0.003883 0.004011
      0.004519 0.005003 0.005511 0.006020 0.006503 0.007012 0.007495 0.008004
      0.008513 0.009021 0.009504 0.010013 0.010522 0.011005 0.011514 0.012023
      0.012506 0.013014 0.013523 0.014006 0.014515 0.015024 0.015507 0.016016
      0.016524 0.017008 0.017516 0.018025 0.018508 0.019017 0.019500 0.020009
      0.020034
```

c

```
sp2 0.000000 0.000685 0.001615 0.001334 0.003231 0.130838 0.020113 0.021465
      0.030780 0.038524 0.045170 0.047979 0.048400 0.048945 0.046724 0.045512
```

0.044151 0.040982 0.037927 0.035899 0.034591 0.030578 0.028787 0.026557
0.023792 0.021448 0.019885 0.017269 0.014907 0.013740 0.012493 0.010658
0.009956 0.008428 0.007506 0.006927 0.005917 0.005206 0.004126 0.003538
0.003415

c

f8:p 2

E8:p 0.000000 0.000001

0.000501 0.001009 0.001518 0.002001 0.002510 0.003044 0.003883 0.004011
0.004519 0.005003 0.005511 0.006020 0.006503 0.007012 0.007495 0.008004
0.008513 0.009021 0.009504 0.010013 0.010522 0.011005 0.011514 0.012023
0.012506 0.013014 0.013523 0.014006 0.014515 0.015024 0.015507 0.016016
0.016524 0.017008 0.017516 0.018025 0.018508 0.019017 0.019500 0.020009
0.020034

c

nps 10000000

REFERENCES

- [1] Environmental Protection Agency (2012). Radiation: Non-Ionizing and Ionizing. *Environmental Protection Agency*. From <<http://www.epa.gov/rpdweb00/understand>>
- [2] Turner, J.E. (1995) *Atoms, Radiation and Radiation Protection*. New York: John Wiley and Sons, Inc.
- [3] International Commission on Radiological Commission (2007). ICRP Publication 103. *Annals of the ICRP 37(2-4)*, 49-79.
- [4] Cooper, J.R., Keith R., and Ranjeet S.S. (2003). *Radioactive Releases in the Environment: Impact and Assessment*. Chichester, West Sussex, England: J. Wiley.
- [5] Martin, E.B.M (1982). *Health Physics Aspects of The Use of Tritium*. London: Science Reviews Limited.
- [6] Thompson, P. (2011). *Darlington New Build Project Joint Review Panel*. Canadian Nuclear Safety Commission. From <<http://www.ceaa.gc.ca/050/documents/49178/49178F.pdf>>
- [7] Boecker, B. "Radiation Effects – Radiation Modifiers." *HPS*. Health Physics Society. From <<http://hps.org/publicinformation/ate/q647.html>>
- [8] Ellett, W.H., Braby, L.A. (1972). The Microdosimetry of 250 kVp and 65 kVp X Rays, ^{60}Co Gamma Rays and Tritium Beta Particles. *Radiation Research*, 51(1972), 229-243.
- [9] Goodhead, D.T. (2009). The relevance of dose for low-energy beta emitters. *Journal of Radiological Protection*, 29(2009), 321-333.
- [10] Harrison, J. (2009). Doses and risks from tritiated water and environmental bound tritium. *Journal of Radiological Protection*, 29(2009), 335-349
- [11] Radiological Tool Box (2006). Computer Software. Version 2.0.0. From <<http://www.nrc.gov/about-nrc/regulatory/research/radiological-toolbox.html>>
- [12] Sprawls, P. (1995). *Physical Principles of Medical Imaging*. United States of America. Medical Physics Pub. Corp.
- [13] MIT Lecture Notes: Introduction to Ionizing Radiation (2006). Interactions of Photons with Matter. *MIT OpenCourseWare*. From

<http://ocw.mit.edu/courses/nuclear-engineering/22-01-introduction-to-ionizing-radiation-fall-2006/lecture-notes/energy_dep_photo.pdf>

- [14] Dunn, W.L., Hugtenburg, R.P. (2006). The Interaction of Radiation with Matter: Charged Particle and Electron Interactions. *CERN IEEE Short Course*. From <http://ab-div-bdi-bl-blm.web.cern.ch/ab-div-bdi-bl-blm/literature/short_course/hugtenburgIEEE2.pdf>
- [15] University of California, Davis. The Electromagnetic Spectrum. *University of California SolarWiki*. From <http://solarwiki.ucdavis.edu/The_Science_of_Solar/1._Basics/B._Basics_of_the_Sun/I._Properties_of_Light/1._The_Electromagnetic_Spectrum>
- [16] Department of Physics and Astronomy. Compton Scattering. *Georgia State University*. From <<http://hyperphysics.phy-astr.gsu.edu/hbase/quantum/comptint.html>>
- [17] X-5 Monte Carlo Team (2008). MCNP – A General Monte Carlo N-Particle Transport Code, Version 5, Volume 1: Overview and Theory. *Los Alamos National Laboratory*.
- [18] NIST (1998). XCOM: Photon Cross Sections Database. *National Institute of Standards and Technology*. From <<http://www.nist.gov/pml/data/xcom/index.cfm>>
- [19] Eisberg, R., Resnick, R. (1985). *Quantum Physics of Atoms, Molecules, Solids, Nuclei, and Particles*. United States of America: John Wiley & Sons, Inc.
- [20] Attix, F.H. (1986). *Introduction to Radiological Physics and Radiation Dosimetry*. United States of America: John Wiley & Sons, Inc.
- [21] NIST (2011). Water. *National Institute of Standards and Technology*. From <<http://webbook.nist.gov/cgi/cbook.cgi?ID=C7732185&Mask=20>>
- [22] Waller, E. (2011). *Introductory MCNP: Using MCNP4A. Monte Carlo Methods Course (Winter 2011)*.
- [23] Hitachi (2013). XRF Analysis. *Hitachi*. From <http://www.hitachi-hitec-science.com/en/products/xrf/tec_descriptions/descriptions_e.html>
- [24] United Performance Metals (2006). Technical Data: Stainless Steels. *United Performance Metals*. From <<http://www.upmet.com/media/302-304-304l-305.pdf>>

- [25] ISNAP (2013). Diagnostic Radiology: Production and Characteristics of X-Rays. *University of Notre Dame Institute for Structure and Nuclear Astrophysics*. From <<http://isnap.nd.edu/Lectures/mphysics/>>
- [26] Bushberg, J.T., Seibert, J.A., Leidholdt, Jr., E.M., Boone, J.M. (2012). *The Essential Physics of Medical Imaging (3rd Edition)*. Philadelphia, Pennsylvania: Lippincott Williams & Wilkins.
- [27] Amptek (2011). Mini-X X-Ray Tube 50 kV USB Controlled User Manual. Amptek, Inc.
- [28] Knoll, G.F. (2000). *Radiation Detection and Measurement (3rd Edition)*. New York: John Wiley and Sons.
- [29] Amptek (2011). *Complete X-Ray Spectrometer with Silicon Drift Detector: User Guide and Operating Instructions*. Amptek, Inc.
- [30] Amptek (2012). X-Ray Tube. Amptek, Inc. From <<http://www.amptek.com/minix.html>>
- [31] Segre, C.U., Bandyopadhyay, P. Periodic Table. From <<http://www.csrrri.iit.edu/periodic-table.html>>
- [32] Pevey, R.E. (1998). *Radiation Protection and Shielding: Photon Interactions (Lecture Notes)*. *University of Tennessee, Knoxville*. From <<http://web.utk.edu/~rpevey/NE406/lesson9.htm>>
- [33] Amptek (2002). X-Ray Fluorescence Spectroscopy. Amptek, Inc. From <<http://www.amptek.com/xrf.html>>
- [34] The Goodfellow Group (2013). Goodfellow On-line Interactive Catalogue. Goodfellow. From <<http://www.goodfellow.com/catalogue/GFCatalogue.php?Language=E>>
- [35] Kortright, J.B. X-Ray Data Booklet: Fluorescence Yields for K and L Shells. From http://xdb.lbl.gov/Section1/Sec_1-3.html
- [36] Biological Effects of Ionizing Radiation Exposure Committee (2006). *Health Risks from Exposure to Low Levels of Ionizing Radiation*. Washington, D.C.: The National Academies Press.